INL/EXT-20-57403
Revision 0

Advanced Reactor Technologies: Very High Temperature Reactor Research and Development Quarterly Report

October, November, December 2019

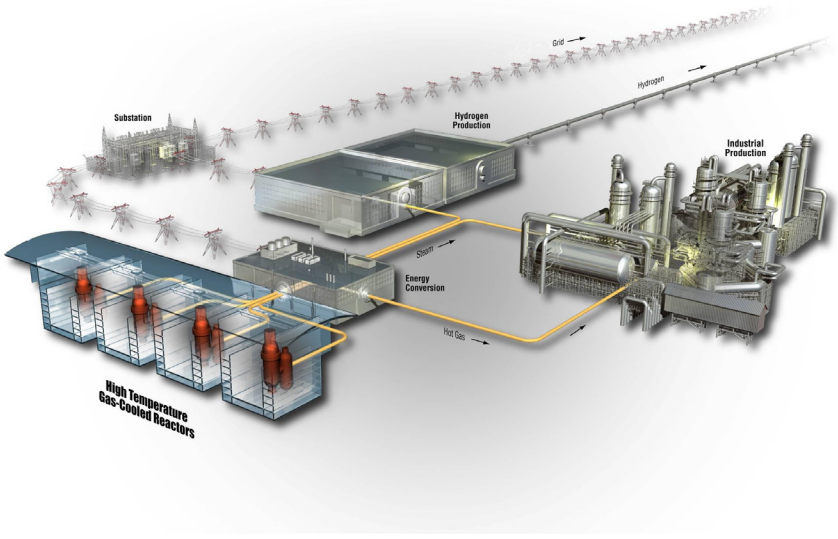

The INL is a
U.S. Department of Energy
National Laboratory
operated by
Battelle Energy Alliance

Idaho National Laboratory

Please note this report contains preliminary data, interim conclusions and observations from work-in-progress.

INL/EXT-20-57403
Revision 0

Advanced Reactor Technologies: Very High Temperature Reactor Research and Development Quarterly Report

October, November, December 2019

Idaho National Laboratory
INL ART Program
Idaho Falls, Idaho 83415

http://www.inl.gov

Prepared for the
U.S. Department of Energy
Office of Nuclear Energy
Under DOE Idaho Operations Office
Contract DE-AC07-05ID14517

INL ART Program

Advanced Reactor Technologies: Very High Temperature Reactor Research and Development Quarterly Report

INL/EXT-20-57403
Revision 0

October, November, December 2019

Approved by:

Travis R. Mitchell
INL ART Program Manager

2/11/2020
Date

CONTENTS

FIGURES

TABLES

ACRONYMS

AGC	Advanced Graphite Creep
AGR	advanced gas reactor
ART	Advanced Reactor Technologies
ASME	American Society of Mechanical Engineers
ATR	Advanced Test Reactor
BLH	Boltzmann-Langmuir-Hinshelwood
BPVC	Boiler and Pressure Vessel Code
BWXT	BWX Technologies
CCL	Carbon Characterization Laboratory
CRP	Coordinated Research Project
CT	computed tomography
CVD	chemical vapor deposition
DOE	Department of Energy
DTF	designed-to-fail
DUF	dispersed uranium fraction
ECAR	engineering calculations and analysis report
EDS	energy dispersive spectroscopy
EKF	exposed kernel fraction
ESR	electro slag remelt
FACS	fuel accident condition simulator
FEM	finite element method
FIB	focused ion beam
FITT	Furnace for Irradiated Tristructural Isotropic (TRISO) Testing
FY	fiscal year
GIF	Generation IV International Forum
GR GCCCCA	Graphite and Ceramic Composite Core Component and Assemblies
HDG	High Dose Graphite Experiment
HFEF	Hot Fuel Examination Facility
HTGR	high temperature gas-cooled reactor
HTM	High Temperature Module
HTR	high temperature reactor
HTTF	High Temperature Test Facility
IAEA	International Atomic Energy Agency

IMCL	Irradiated Materials Characterization Laboratory
IMGA	irradiated microsphere gamma analyzer
I-NERI	International Nuclear Energy Research Initiative
INL	Idaho National Laboratory
IPyC	inner pyrolytic carbon
KAERI	Korea Atomic Energy Research Institute
LBL	leach-burn-leach
LEU	low-enriched uranium
LH	Langmuir-Hinshelwood
MAD	median and median absolute deviation
MCNP	Monte Carlo N-Particle
NCSU	North Carolina State University
NDM	Nonmetallic Design and Materials
NEA	Nuclear Energy Agency
NRAD	Neutron Radiography Reactor
NRC	Nuclear Regulatory Commission
NTB	Nonmetallic Design and Materials
OPyC	outer pyrolytic carbon
ORN	Oak Ridge National Laboratory
OSU	Oregon State University
PED	precision electron diffraction
PF	packing fractions
PGS	Precision Gamma Scanner
PIE	post-irradiation examination
PNNL	Pacific Northwest National Laboratory
R-DLBL	radial deconsolidation-leach-burn-leach
S/A	solution annealed
SCALE	Standardized Computer Analyses for Licensing Evaluation
SDF	SiC defect fraction
SiC	silicon carbide
STEM	scanning transmission electron microscopy
TAG	A dual symmetrical thermogravimetric analyzer
TEM	transmission electron microscopy
TRISO	tristructural isotropic
UAM	Uncertainties in Modeling

UCO	uranium carbide/oxide
VHTR	very hig -temperature reactor
WG	working group
XCT	x-ray computed tomography

Advanced Reactor Technologies: Very High Temperature Reactor Research and Development Quarterly Report

1. MAJOR ACCOMPLISHMENTS

1.1 Fuels Development Qualification

Highlights of Advanced Gas Reactor (AGR) fuels-development activities during October, November, and December 2019 are as follows:

October

- Completed burn-leach and analysis of leachates for particles from 1500°C safety-tested AGR-2 UO_2 Compact 3-1-1.
- Completed burn-leach of particles from as-irradiated AGR-2 UO_2-Compact 3-1-2 and analysis of leachates is in progress.
- Completed gamma counting with the Irradiated Microsphere Gamma Analyzer (IMGA) of particles from as-irradiated AGR-2 UO_2 Compact 3-1-2.
- Completed gamma counting with the IMGA of ten burned-back particles from as-irradiated AGR-2 uranium oxide (UCO) Compact 5-4-2 for heating tests in the Furnace for Irradiated TRISO Testing (FITT).
- Completed x-ray tomography of select particles recovered from 1800°C safety-tested AGR-2 UCO Compact 6-2-1.
- Completed cross sectioning of randomly selected particles from 1500°C safety-tested AGR-2 UO_2 Compact 3-1-1 and special particles from 1800°C safety-tested AGR-2 UCO Compact 6-2-1.
- Completed radiochemical analyses of the solutions from deconsolidation-leach-burn-leach (DLBL) of AGR-2 Compact 6-4-1.
- Completed re-irradiation in the Neutron Radiography Reactor (NRAD), gamma scanning on the Precision Gamma Scanner (PGS), and subsequent 1200°C test in the Fuel Accident Condition Simulator (FACS) furnace AGR-3/4 Compact 8-1.
- Completed three-step temperature cycling test of AGR-3/4 Compact 8-1 after the 1200°C test in order to investigate possible bursts of Kr-85 and Xe-133 during temperature transients.
- Received all gamma, Sr-90, and inductively coupled plasma mass spectrometry data from Pacific Northwest National Laboratory's analysis of the samples from AGR-3/4 Capsule 10 inner and outer rings.
- Epoxied the AGR-3/4 Capsule 12 inner and outer rings for destructive physical sampling.
- Completed EDS for elemental analysis of fission-product redistribution in randomly selected particles from 1600°C safety-tested AGR-2 UCO Compact 5-2-1 and 1800°C safety-tested AGR-2 UCO Compact 6-2-1.
- Completed the transmission electron microscopy (TEM) analysis including scanning TEM (STEM), precision electron diffraction, and EDS on TRISO particle AGR2-22-RS027.
- Received shipment of single-piece alumina tubes and segmented alumina tubes for the Air/Moisture Ingress Experiment.

- Transferred natural uranium TRISO particles to the Irradiated Materials Characterization Laboratory (IMCL) for x-ray computed tomography (CT).
- Shipped over 400 natural uranium fuel compacts from BWXT with nominal packing fractions of 25% and 40%.
- Identified 88 kg of the residual uranium materials at BWXT for disposal and 52 kg to be shipped to INL for storage. The disposition of another 25 kg of uranium is yet to be determined.

November

- Completed 100-h testing at 1600°C of particles from AGR-2 UCO Compact 5-4-2 in the Furnace for Irradiated TRISO Testing (FITT).
- Completed analysis of leachates from burn-leach of particles from as-irradiated AGR-2 UO2-Compact 3-1-2.
- Completed burn-leach and radiochemical analysis of the graphite holders from the second re-irradiation and FACS heating test (1400°C) of cracked particles from AGR-2 Compact 5-4-2.
- Completed radiochemical analysis of the condensation plates from third re-irradiation and FACS heating test (1200°C) of cracked particles from AGR-2 Compact 5-4-2.
- Completed radiochemical analysis of all samples generated from the radial deconsolidation of AGR-3/4 Compact 7-3.
- Submitted report (Oak Ridge National Laboratory (ORNL)/TM-2019/1341), "Oxidation of Matrix Material in Helium with Varied Moisture Content."
- Submitted report (ORNL/TM-2019/1154), "Additional Confirmatory LBL Analysis of AGR-5/6/7 Compacts and Overcoated Particles."
- Completed TEM data analysis on particle AGR2-222-RS019.
- INL hosted a meeting of the AGR program Technical Coordination Team including AGR personnel from ORNL.
- Transferred approximately 22 grams of natural uranium TRISO particles to NASA to demonstrate TRISO fuel robustness for the NASA Nuclear Propulsion program.
- Continued irradiation of AGR-5/6/7 in Advanced Test Reactor (ATR). Completed 4590 MWd's (megawatt-days).
- Initiated fabrication process for consumable items required to size and ship AGR-5/6/7.

December

- Progressed on preparations to ship some low-enriched uranium materials from the AGR program at BWX Technologies (BWXT) to INL for archival and to support other research activities.
- Identified storage locations for storing the low-enriched uranium (LEU) fuel at INL.
- Completed 500-h testing at 1600°C of particles from AGR-2 UCO Compact 5-4-2 in the FITT.
- Completed impact cracking of five particles from irradiated AGR-2 Compact 2-2-1 for re-irradiation and safety testing at INL, x-ray analysis is delayed until repair of tomograph.
- Submitted paper to Journal of Nuclear Materials on "Role of Microstructure on CO Corrosion of SiC layer in UO2-TRISO fuel."

- Submitted paper to Journal of Nuclear Materials on "Redistribution of Radionuclides in Irradiated AGR-1 UCO TRISO Fuel after 1800°C Safety-Testing."
- Completed irradiated fuels and materials oxidation test plan (PLN-5934, INL/MIS-17-43986) "AGR Irradiated Specimen Air/Moisture Heating Test Plan".
- Completed destructive physical sampling of AGR-3/4 Capsule 12 inner and outer rings at Hot Fuel Examination Facility (HFEF).
- Began rebuilding the FACS furnace internals in preparation for heating tests planned this fiscal year.
- Began x-ray CT of natural uranium TRISO particles at the IMCL in preparation for irradiated particle x-ray CT.
- Transferred natural uranium TRISO particles to IMCL for plasma focused ion beam (FIB) milling.
- Completed functional and operational requirements document (FOR-505) "AGR-5/6/7 Disassembly System", and contracted Walsh Engineering to assist in designing equipment for AGR-5/6/7 Post-Irradiation Examination (PIE).
- INL staff attended a Nuclear Regulatory Commission (NRC) public meeting related to the recent topical report on UCO TRISO fuel performance submitted to the NRC. INL staff lead the technical discussion of the proposed responses to NRC Requests for Additional Information.

1.2 High-Temperature Materials Development

Highlights of high-temperature materials activities during October, November, and December 2019 are as follows:

October

- Participated at the October 2019 American Society of Mechanical Engineers (ASME) Boiler and Pressure Vessel Code Week.
- Reloaded a base-metal Alloy 617 V-notch specimen and restarted short-term creep-rupture testing (800°C, 65.3 MPa). The expected life is 4,800 hours. The test is currently at 2,230 hours.
- Characterized the base-metal Alloy 617 V-notch creep-rupture (800°C, 65.3 MPa) specimen that was interrupted at 2,005 hours using x-ray CT.
- Started and sustained creep-rupture testing (850°C, 54 MPa) of an Alloy 617 small-radius weld-metal Bridgeman-notch specimen. The test has been running for 13 hours.
- Started and sustained intermediate creep-rupture testing (800°C, 60 MPa) of an Alloy 617 large-radius base-metal Bridgeman-notch specimen. The test has been running for 326 hours.
- Sustained intermediate creep-rupture testing (800°C, 60 MPa) of an Alloy 617 small-radius base-metal Bridgeman-notch specimen. The test has been running for 857 hours.
- Sustained intermediate creep-rupture testing (900°C, 28 MPa) of an Alloy 617 small-radius base-metal Bridgeman-notch specimen. The test has been running for 1,326 hours.
- Sustained intermediate creep-rupture testing (900°C, 28 MPa) of an Alloy 617 large-radius base-metal Bridgeman-notch specimen. The test has been running for 1,335 hours.
- Sustained intermediate creep-rupture testing (900°C, 28 MPa) of an Alloy 617 small-radius weld-metal Bridgeman-notch specimen. The test has been running for 1,054 hours.
- Sustained intermediate creep-rupture testing (900°C, 28 MPa) of an Alloy 617 large-radius weld-metal Bridgeman-notch specimen. The test has been running for 1,135 hours.

- Quantified creep damage for the small- and large-radius base-metal Bridgeman-notch creep-rupture specimens. The fraction of voids in each row and column of pixels was determined.
- Measured grain size as a function of distance from the weld for the as-received Alloy 800H welded plate with Alloy 617 filler. Grain size in the base-metal was not observed to change with distance from the weld. The American Society for Testing and Materials (ASTM) grain size number of the Alloy 800H base-metal is 2.
- Analyzed INL's and the Korean Atomic Energy Research Institute's (KAERI) diffusion-welded creep-rupture data. The stress-rupture factors were evaluated. The n value from the phenomenological equation for steady state creep and the creep activation energy were calculated.
- Sent KAERI INL's contributions to the I-NERI 2016-002-K, Demonstration of Diffusion Bonding Performance of Alloy 617 for the Application of Compact Heat Exchange, for project reporting.

November

- CT characterization. The expected life is approximately 4,800 hours. The test was interrupted at 2,500 hours.
- Characterized the baseline creep-rupture test (800°C, 65.3 MPa) of a base-metal V-notch specimen interrupted at 2,500 hours with x-ray CT.
- Inspected the four Alloy 617 welded plates with Alloy 617 filler using radiography at two different angles.
- Plotted the diffusion-welded data on the Alloy 617 D-diagram.
- Prepared and sent slides to KAERI on INL's contributions to the I-NERI 2016-002-K, Demonstration of Diffusion Bonding Performance of Alloy 617 for the Application of Compact Heat Exchanger for the reporting of this project.

December

- Drafted and officialized an engineering drawing for a specimen comprised of two V-notches labeled a double V-notch specimen.
- Sectioned off a piece of an Alloy 617 plate for the machining of base-metal double V-notch specimens.
- Submitted an iBuy request to have cyclic weldment and weld-metal V-notch specimens machined from two of the Alloy 617 welded plates with Alloy 617 filler.
- Started and sustained creep-rupture testing (850°C, 54 MPa) of a diffusion-welded Alloy 617 specimen from the center of the plate. The test is currently at 182 hours.

1.3 Graphite

Highlights of graphite activities during October, November, and December 2019 are as follows:

October

- Continued irradiation of the Advanced Graphite Creep (AGC)-4 experiment. This is the last of eight planned irradiation cycles.
- Proceeded with preparations for sizing and shipping of AGC-4 Capsule after completion of irradiation.
- Initiated final plans for High Dose Graphite Experiment (HDG-1) assembly in preparation for reactor insertion.

- Performed multiple simulations to study the variability in mechanical strength produced by variation in the pore distribution. Pore diameters were lognormally distributed and randomly placed throughout the domain. The distribution of maximum stresses showed the same trends as those found experimentally.
- Began exploring the applicability and utility of various optical methods, including sub diffraction limit imaging, for characterizing nano-scale defects in graphite.
- Completed draft of "Standard Guide for Evaluation of Nuclear Graphite Surface Area and Porosity by Gas Adsorption Measurements" and shared it with external specialists in the field.
- Retrieved 72 previously tested Mersen Grade 2114 ATTM C749 type 109 (reduced diameter) specimens for use in machining 6-mm-diameter x 3-mm-thick specimens for trial Brazilian Disc testing. Specimen machining will start when new fiscal year (FY)-20 funding is received.
- Attended and led two ASME Boiler and Pressure Vessel Code (BPVC) working groups: (i) on General Requirements for Graphite and Ceramic Composite Core Component and Assemblies (GR GCCCCA) and (ii) the Nonmetallic Design and Materials. The nonmetallic working group agreed to undertake a major modification to the graphite sections of the ASME Code Companion Guide, modifying the graphite/composite code to change all "fluence" references to a "dose or dpa (displacements per atom)," and completed a number of minor editorial and technical modifications to the 2021 BPVC version. In addition, the nonmetallic working group will hold a bi-annual meeting with nonmetallic vendors/designers to discuss specific nonmetallic component questions and issues.
- Presented status of the graphite ASME-NRC Roadmap at the ASME BVP code week (October 27 - November 1, 2019). A final draft of the Design Basis Report (minus two key open literature references) is complete while the first draft of the Gap Analysis Report is complete. Drafts of both reports will be furnished to the NRC for consideration during their Section 3, Division 5 acceptance assessment.
- Commenced review of ASME "Division 5 Nonmetallic Rules Background" draft document. The suggestion was made to the BPV III executive committee to convert the document to a Nuclear Technical Book (NTB). The motion was endorsed by the committee.

November

- Submitted 24 grade 2114 (an isotropic graphite) ASTM C749 type 109 broken specimens to the shop to machine two discs (6 mm diameter x 3 mm thickness) per test bar. The discs will provide a comparison of the new ASTM method for tensile strength from disc compression and ASTM C749. Duplicate samples will be used for determining the effects of chronic oxidation on strength.
- Ran multiple simulations of mechanical strength, parametrized from the literature for graphite grade H-451. The maximum stress distribution was found to match well with experimental results.
- Established HDG-1 specimen loading order and completed pre-campaign examination of specimens.
- Completed HDG-1 capsule specimen holder machining in preparation for experiment assembly.
- Loaded HDG-1 specimens (both previously irradiated and new) into polycarbonate tubes (14 each) at the INL-Carbon Characterization Laboratory (CCL). These tubes will be shipped to the capsule assembly facility at the Test Train Assembly Facility. During capsule assembly, the specimens will be inserted directly into the HDG-1 Capsule in the correct order by sliding each group of specimens from the poly tube directly into the capsule specimen holder.
- Attended the Fall ASME Code Week meeting (October 27–November 1, 2019) in support of graphite and ceramic composite code development. Two draft reports for the ASME/NRC Roadmap activity—

the Gap Analysis Report and Design Basis Document—have been completed with public release pending finalization.

- Attended and chaired the International Atomic Energy Agency (IAEA) Technical Meeting on the Status of the IAEA Nuclear Graphite Knowledge Base, held in Vienna, November 7–8, 2019. This database is the storehouse for much of the historical nuclear graphite data available from numerous countries including the US, European Union, United Kingdom, Russia, and elsewhere. During this meeting, the Nuclear Graphite Knowledge Base was approved for uploading into the Generation IV International Forum (GIF) Handbook.

December

- Examined dimensions of one of each pair of the 48-disc specimens machined from the heads of 24 type 109 ASTM C749 (dog-bone) broken tensile specimens in accordance with ASTM D8289 (Tensile Strength Estimate by Disc Compression).
- Ran mechanical model simulations for graphite grade NBG-8 by utilizing experimentally determined pore and filler distribution parameters.
- Attended ASTM Meeting (D2 Petroleum Products, Liquid Fuels, and Lubricants) December 8–12, 2019, in New Orleans, Louisiana, addressing graphite testing relevant to nuclear applications in updates and new standards under consideration.
- Presented and participated in NRC event: Advanced Non-Light Water Reactors – Materials & Component Integrity Workshop, December 9–11, 2019, in Washington, DC.
- Issued baseline testing engineering calculations and analysis report (ECAR) "Baseline Characterization Database Verification Report – IG110 Billet 10X69" (Level 2 Milestone) in advance of the January 15, 2020, due date.
- Issued baseline testing ECAR "Baseline Characterization Database Verification Report – 2114 Billet A20570" (Level 2 Milestone) in advance of the January 15, 2020, due date.

1.4 GRC Modeling & Validation

Highlights of methods activities during October, November, and December 2019 are as follows:

October

- Received the qualified data from the Oregon State High Temperature Test Facility (HTTF) for two tests. The first is a pressurized conduction cooldown and the second is a depressurized cooldown.
- Initiated the development of methodology for normal and transient analysis simulation of pebble bed reactor a few-group temperature, burnup, and spectrum dependent cross-section generation. The methodology will be presented either at the High Temperature Reactor (HTR) 2020 conference or as a journal article.
- Completed the Phase IV coupled control rod withdrawal transient simulations for the IAEA Coordinated Research Projects (CRP) on high temperature gas-cooled reactor (HTGR) Uncertainties in Modeling (UAM). The uncertainty and sensitivity assessment of these transients will be reported in the 2020 draft IAEA TECDOC.
- Completed the coupled steady state uncertainty assessment defined for Phase III of the IAEA CRP on HTGR Uncertainties.

November

- Attended the Technical Working Group meeting on HTGRs in IAEA headquarters in Vienna
- Attended the Technical Meeting on the Competitiveness and Early Deployment of Small Modular Reactors and High Temperature Gas-Cooled Reactors in IAEA Headquarters in Vienna

- Continued the planning of the development of pebble bed reactor few-group temperature, burnup and spectrum dependent cross-section generation methodology for normal and transient analysis simulation.

December

- Initiated discussions with INL property Management organization and Oregon State University (OSU) about transferring the process to transfer the HTTF equipment to OSU.
- Continued the INL contributions to the IAEA TECDOC on the IAEA CRP on HTGR Uncertainties in Modeling (UAM) and the OECD/NEA MHTGR-350 benchmark comparison report.

2. SIGNIFICANT ACCOMPLISHMENTS

2.1 Fuels Development and Qualification

2.1.1.1 LBL Analysis of AGR-5/6/7 Compacts and Overcoated Particles

Two series of leach-burn-leach (LBL) analyses of the AGR Program's AGR-5/6/7 irradiation test fuel have been performed at ORNL to gather additional data in support of irradiation testing and PIE and to confirm results from similar analyses performed by BWXT NOG. The first test series was completed in FY-18 and results were reported in ORNL/TM-2018/744 (Hunn et al. 2018). Analysis of these results identified several possible discrepancies in the available data sets and some data sets that required additional sampling to provide sufficient statistics for comparison and refined conclusions. The second test series was completed in FY-19 and results were reported in ORNL/TM-2019/1154 (Hunn et al. 2019). This second report provided a combined analysis of the two-test series and comparative analysis with previous BWXT NOG results, and portions of the report are duplicated herein to provide a summary of the ORNL results.

Fuel compacts for the AGR-5/6/7 irradiation test were fabricated by BWXT NOG at their facility in Lynchburg, Virginia. Two compact packing fractions (PFs) were produced—nominally, 40% PF and 25% PF—in which the TRISO-coated particle volume was targeted to be 40% and 25% of the total compact volume, respectively. Both compact lots used TRISO particles from the same composite. The TRISO coatings were deposited using a 150 mm diameter fluidized-bed chemical vapor deposition (CVD) furnace on spherical kernels that were nominally 425 μm in diameter. The kernels were from kernel composite Lot J52R-16-69317, which contained LEU (15.5% ^{235}U) in a mixture of uranium carbide and UCO. Kernels were coated with four concentric CVD layers: a porous carbon buffer layer that was nominally 100 μm thick, an inner pyrolytic carbon (IPyC) layer that was nominally 40 μm thick, a silicon carbide (SiC) layer that was nominally 35 μm thick, and an outer pyrolytic carbon (OPyC) layer that was nominally 40-μm-thick. Coated particle composite J52R-16-98005 was overcoated (OC) with a graphite/resin blend, and these OC TRISO particles were pressed to form cylindrical compacts that were nominally a half inch in diameter and one inch long.

Compact samples were deconsolidated and analyzed using the LBL procedure at ORNL to provide additional data for use in evaluating the compact properties previously measured by LBL analysis at BWXT NOG. In addition, samples of OC TRISO particles were analyzed by LBL at ORNL to distinguish possible changes in defect fractions that result from (1) the OC process (by comparison to non-OC TRISO particle LBL) and (2) the compacting process (by comparison to compact LBL). Table 1 lists the samples analyzed at ORNL. Results of the LBL analyses include the exposed kernel fraction (EKF), the SiC defect fraction (SDF), and the dispersed uranium fraction (DUF). The definitions and calculations used to determine EKF, SDF, and DUF are explained in ORNL/TM-2019/1154 (Hunn et al. 2019).

Table 1. Samples analyzed at ORNL

Test Series	Nominal PF	Batch ID	Description	Analysis
1	40%	J52R-16-14154C	40 compacts	LBL in 2 groups of 4 clutches of 5 compacts
2	40%	J52R-16-14154C	20 compacts	LBL in 1 group of 4 clutches of 5 compacts
2	40%	J52R-16-14155C	40 compacts	LBL in 2 groups of 4 clutches of 5 compacts
1	25%	J52R-16-14156C J52R-16-14156D	29 compacts 11 compacts	LBL in 2 groups of 4 clutches of 5 compacts [a]
2	25%	J52R-16-14156D	20 compacts	LBL in 1 group of 4 clutches of 5 compacts
1	40%	J52R-16-11034	OC TRISO	LBL in 2 groups of 4 clutches of OC TRISO [b]
2	40%	J52R-16-11035	OC TRISO	LBL in 2 groups of 4 clutches of OC TRISO [b]

Note: Each 5-compact clutch was randomly chosen.
[a] The 25% PF compacts in the first test series were from production batches 14156C and 14156D.
[b] OC TRISO clutches were random samples with roughly the same number of particles as a 5-compact clutch.

2.1.1.1.1 Results for Overcoated Particles

Table 2 shows details regarding the uranium (in kernel equivalents) in each solution collected during preburn leaching of the OC TRISO clutches and the total uranium leached from each clutch. According to procedure, the water rinse data were not included in the total because they were ≤10% of the second leach or ≤1% of the average uranium per kernel. Table 2 also shows the individual preburn leach DUFPre values for each clutch without an exposed kernel defect (i.e., the total leached uranium was <0.5 kernel equivalents per the AGR-5/6/7 Fuel Specification).

Table 3 shows the same type of data for the postburn leach. The DUFPre and DUFPost values were very consistent in the preburn and postburn clutches, respectively, and the uranium content in each second leach was appropriately lower than the first leach. These observations are good indicators that the LBL process was effective.

Table 4 summarizes the dispersed uranium analysis results for OC TRISO Batch 11034 and Batch 11035 separately and considered as a pooled data set. The mean and standard deviations for DUF_{Pre} and DUF_{Post} come from the individual clutch values reported in Table 2 and Table 3, respectively.

The 95% confidence limits in

Table 4 are the upper bounds of the 95% confidence interval of the mean value for the sampled material based on the measured sample. The DUF_{Pre} and DUF_{Post} 95% confidence limits were calculated using the Student's t-test. The DUF_{Total} mean value was calculated by adding the DUF_{Pre} and DUF_{Post} mean values as stipulated in the AGR-5/6/7 Fuel Specification, and the 95% confidence limit was determined from approximations of the cumulative probability distributions for DUF_{Pre} and DUF_{Post} as described in ORNL/TM-2019/1154 (Hunn et al. 2019). The DUF results from the two OC TRISO batches were very similar, so pooling the data to provide better statistical sampling appears to be justified. Approximately 96% of the total dispersed uranium was leached in the preburn leaches.

Table 2. Uranium leached from 40% PF OC TRISO before the burn

Series	Clutch	Particles	First leach	Second leach	H_2O rinse [a]	Total	DUF_{Pre} [b]
1	11034-1	17,627	7.92E-2	1.05E-2	6.36E-4	0.090	5.09E-6
	11034-2	18,614	8.03E-2	1.61E-2	9.27E-4	0.096	5.18E-6
	11034-3	17,972	8.06E-2	1.10E-2	7.25E-4	0.092	5.10E-6
	11034-4	17,826	7.88E-2	1.85E-2	9.78E-4	0.097	5.46E-6
2	11035-1	17,409	8.33E-2	4.66E-3	2.84E-4	0.088	5.05E-6
	11035-2	17,368	8.23E-2	3.63E-3	1.44E-4	0.086	4.94E-6
	11035-3	17,369	8.20E-2	4.10E-3	1.31E-4	0.086	4.96E-6
	11035-4	17,378	7.95E-2	5.84E-3	1.82E-4	0.085	4.91E-6
	11035-5	17,389	8.20E-2	7.38E-3	2.69E-4	0.089	5.14E-6
	11035-6	17,364	7.79E-2	6.01E-3	2.30E-4	0.084	4.83E-6
	11035-7	17,395	8.77E-2	4.14E-3	1.05E-4	0.092	5.28E-6
	11035-8	17,371	8.57E-2	4.50E-3	1.23E-4	0.090	5.20E-6

Note: Uranium content in each leach is reported in kernel equivalents.
[a] Gray shading indicates that the water rinse was not added to the total.
[b] Individual DUF_{Pre} is the preburn leach fraction of exposed uranium in each clutch with <0.5 exposed kernel equivalents.

Table 3. Uranium leached from 40% PF OC TRISO after the burn

Series	Clutch	Particles	First leach	Second leach	H_2O rinse [a]	Total	DUF_{Post} [b]
1	11034-1	17,627	2.38E-3	1.34E-3	not done	0.004	2.11E-7
	11034-2	18,614	2.58E-3	3.56E-4	not done	0.003	1.58E-7
	11034-3	17,972	3.01E-3	5.52E-4	not done	0.004	1.98E-7
	11034-4	17,826	1.23E+0	3.47E-3	not done	1.234	---
2	11035-1	17,409	1.56E-3	5.54E-4	1.38E-5	0.002	1.21E-7
	11035-2	17,368	1.66E-3	9.69E-4	1.58E-5	0.003	1.51E-7
	11035-3	17,369	1.83E-3	4.68E-4	2.03E-5	0.002	1.32E-7
	11035-4	17,378	2.10E-3	2.60E-4	3.57E-5	0.002	1.36E-7
	11035-5	17,389	1.72E-3	3.75E-5	1.02E-6	0.002	1.01E-7
	11035-6	17,364	3.60E-3	9.56E-5	1.02E-6	0.004	2.13E-7
	11035-7	17,395	1.01E+0	4.37E-3	1.72E-5	1.013	---
	11035-8	17,371	8.06E-3	1.75E-4	9.80E-6	0.008	4.74E-7

Note: Uranium content in each leach is reported in kernel equivalents.
[a] Gray shading indicates that the water rinse was not added to the total.
[b] Individual DUF_{Post} is the postburn leach fraction of exposed uranium in each clutch with <0.5 exposed kernel equivalents.

Table 4. Dispersed uranium in 40% PF OC TRISO

Batch		DUF_{Pre}	DUF_{Post}	DUF_{Total}
11034	Measured mean	5.20E-6	1.89E-7	5.39E-6
	Standard deviation	1.73E-7	2.78E-8	---
	95% confidence limit	≤ 5.41E-6	≤ 2.37E-7	≤ 5.62E-6
11035	Measured mean	5.04E-6	1.90E-7	5.23E-6
	Standard deviation	1.55E-7	1.30E-7	---
	95% confidence limit	≤ 5.15E-6	≤ 2.86E-7	≤ 5.38E-6
Pooled	Measured mean	5.09E-6	1.90E-7	5.28E-6
	Standard deviation	1.73E-7	1.07E-7	---
	95% confidence limit	≤ 5.19E-6	≤ 2.52E-7	≤ 5.40E-6

Table 5 presents the EKF and SDF values calculated from the data presented in Table 2 and Table 3, respectively. Again, results are provided for Batches 11034 and 11035 separately and as a pooled data set. The 95% confidence limits in Table 5 correspond to the true defect fractions in the sampled population that yield a cumulative binomial distribution value of 0.95 for the observed number of defects and sample size. These values are the lowest tolerance limits for which the compact lot would be deemed acceptable at 95% confidence, based on the sample that was measured. There is no strong evidence for a significant difference in EKF and SDF in Batches 11034 and 11035, and given that they were processed similarly, it is reasonable to assume that pooling the data is justified. There were no exposed kernels detected in the preburn leach solutions. Zero exposed kernel defects in a pooled sample of 211,082 OC particles satisfies an upper limit on the EKF in the OC TRISO composite of ≤1.42E-5 with 95% confidence. Based on the prescribed data analysis methods in the fuel specification, there were two exposed kernels detected in the postburn leach solutions, which satisfies to a 95% confidence an upper limit on the SDF in the OC TRISO composite of ≤2.99E-5.

Table 5. Defect fractions in 40% PF OC TRISO

Batch		EKF	SDF
11034	Number of defects	0	1
	Number of particles	~72,039	~72,039
	Measured defect fraction	0	1.39E-5
	95% confidence limit	≤ 4.16E-5	≤ 6.59E-5
11035	Number of defects	0	1
	Number of particles	~139,043	~139,043
	Measured defect fraction	0	7.19E-6
	95% confidence limit	≤ 2.16E-5	≤ 3.42E-5
Pooled	Number of defects	0	2
	Number of particles	~211,082	~211,082
	Measured defect fraction	0	9.47E-6
	95% confidence limit	≤ 1.42E-5	≤ 2.99E-5

The amount of uranium leached from Clutch 11035-7 after the burn was 1.013 kernel equivalents, which strongly supports a conclusion that the uranium came from a single particle with an exposed kernel defect. The amount of uranium leached from Clutch 11034-4 was 1.234 kernel equivalents, which is uncharacteristically high for a typical LBL analysis involving one defective particle. Possible explanations include (1) higher than normal error in the mass spectrometry, (2) the presence of more than one particle with an exposed kernel defect in conjunction with incomplete leaching, and (3) one particle with an exposed kernel defect that had abnormally high uranium content. Incomplete leaching is unlikely given the low uranium content in the second postburn leach. The possibility that a single defective particle contained an abnormally high amount of uranium is likely given the observation of particles with additional kernel material in samples from the AGR-5/6/7 TRISO particle composite and from the individual TRISO particle batches that were blended to form the composite (Helmreich et al. 2017a, Helmreich et al. 2017b). In the x-ray analysis of 241,822 particles from the AGR-5/6/7 TRISO particle composite, six particles with additional kernel material were identified. The additional kernel material was related to the inclusion of fragments of fractured kernels that were bonded to the main kernel prior to coating or trapped in the buffer layer during coating. Figure 1 and Figure 2 show examples. Because the embedded fragments produce abnormal shapes and dispersed uranium in the coating layers, there may be a greater chance that particles of this type will also have coating defects.

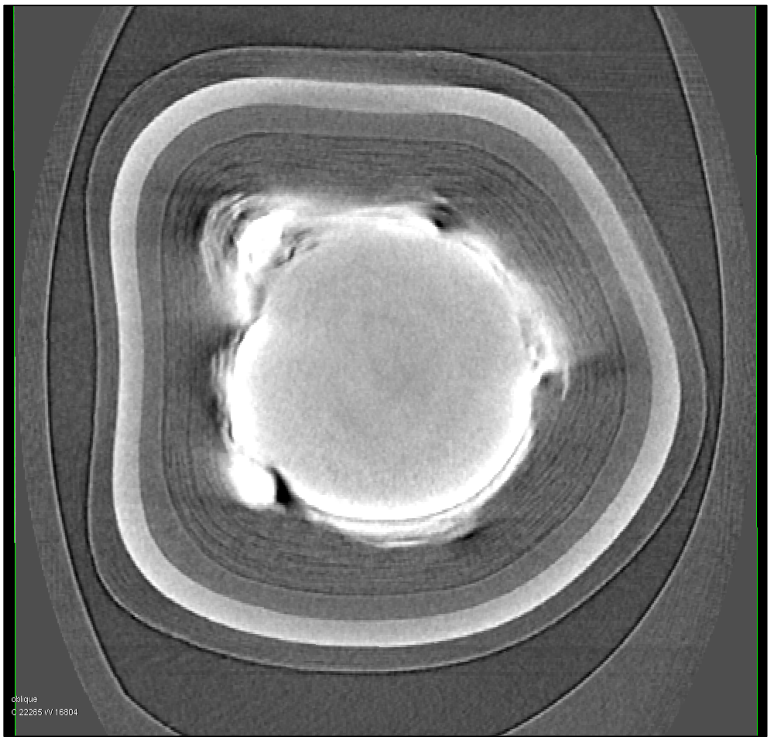

Figure 1. Tomographic cross-section of a particle from Batch 93168 with embedded kernel fragments and uranium dispersion in the buffer layer (Helmreich et al. 2017b, Figure 2-12).

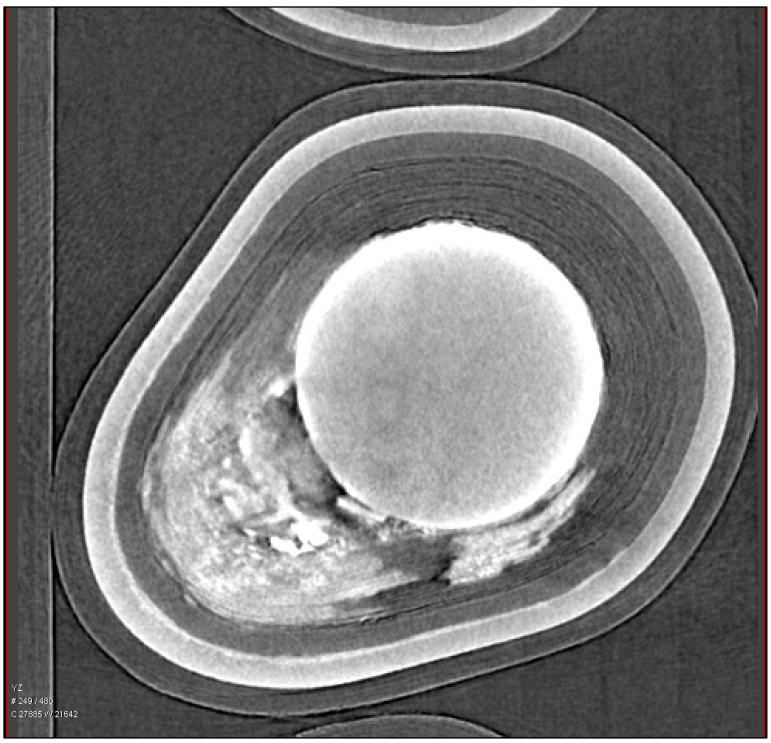

Figure 2. Tomographic cross-section of a particle from Batch 93172 with embedded kernel fragments and uranium dispersion in the buffer layer (Helmreich et al. 2017b, Figure 2-11).

The OC TRISO particles in Batches 11034 and 11035 were made from a composite of four coated particle batches, BWXT NOG Composite J52R-16-98005. The TRISO particles from Composite 98005 were analyzed with LBL by BWXT NOG, and the DUF, EKF, and SDF results reported in INL/EXT-18-45110 (Marshall 2018) are shown in Table 6. The measured values and 95% confidence upper limits for the TRISO particles prior to overcoating are higher than what was determined for the pooled data from the ORNL LBL analysis of the OC TRISO particles (Table 4 and Table 5). This leads to the reasonable conclusion that the overcoating process did not significantly increase the EKF and SDF already present in the TRISO particle feedstock. The limited available information regarding the DUF_{Total} of TRISO Batch 98005 precludes detailed comparison to the OC TRISO, but since the measured mean DUF_{Total} for the TRISO is roughly double that for the OC TRISO, there is no evidence that DUF increased during overcoating either.

Table 6. Defect fractions in TRISO particle Lot 98005 prior to overcoating (Marshall 2018)

	DUF_{Total}	EKF	SDF
Number of defects	---	3	3
Number of particles	---	~319,000	~159,000
Measured defect fraction	1.04E-5	9.40E-6	1.89E-5
95% confidence limit	*a*	≤ 2.43E-5	≤ 4.88E-5

[a] No 95% confidence value was available for DUF because only one of the three postburn leach samples had no exposed kernels.

2.1.1.1.2 Results for 25% PF Compacts

Table 7 shows the amounts of uranium (in kernel equivalents) detected in the solutions collected during preburn leaching of the 25% PF compact clutches, and Table 8 shows similar data for the postburn leaching. The values for total uranium leached from each clutch do not include the water rinse data except for the preburn leach total for Clutch 14156C/D-6, which met the criteria for inclusion because the uranium detected in the water rinse was >10% of the second leach and >1% of the average uranium per kernel. The elevated uranium content in the preburn water rinse of 1.56E-2 in Clutch 14156C/D-6 indicates that leaching of exposed uranium may not have been complete. Clutch 14156C/D-6 was also the only clutch in which a preburn leach exposed kernel defect was detected based on the AGR-5/6/7 Fuel Specification definitions. Table 7 shows the individual preburn leach DUF_{Pre} values for the other clutches in which the preburn leached uranium was <0.5 kernel equivalents. Similarly, Table 8 shows the DUF_{Post} values for the clutches with <0.5 kernel equivalents in the postburn leach solutions.

Table 7. Uranium leached from 25% PF compacts before the burn

Series	Clutch	Particles [a]	First leach	Second leach	H_2O rinse [b]	Total	DUF_{Pre} [c]
1	14156C/D-1	11,465	3.66E-2	6.77E-3	6.56E-4	0.043	3.79E-6
	14156C/D-2	11,465	2.90E-2	6.01E-3	6.18E-4	0.035	3.05E-6
	14156C/D-3	11,465	1.87E-1	2.87E-2	2.98E-3	0.216	1.88E-5
	14156C/D-4	11,465	6.74E-2	8.13E-3	1.17E-3	0.076	6.59E-6
	14156C/D-5	11,465	4.12E-2	4.75E-3	7.66E-4	0.046	4.00E-6
	14156C/D-6	11,465	8.70E-1	6.29E-2	1.56E-2	0.949	---
	14156C/D-7	11,465	2.81E-2	2.96E-3	4.53E-4	0.031	2.71E-6
	14156C/D-8	11,465	3.15E-2	5.78E-3	8.55E-4	0.037	3.26E-6
2	14156D-1	11,465	3.75E-2	3.91E-3	1.88E-4	0.041	3.61E-6
	14156D-2	11,465	3.88E-2	5.00E-3	2.41E-4	0.044	3.82E-6
	14156D-3	11,465	4.80E-2	4.34E-3	2.36E-4	0.052	4.56E-6
	14156D-4	11,465	3.07E-2	3.13E-3	1.65E-4	0.034	2.95E-6

Note: Uranium content in each leach is reported in kernel equivalents.

[a] The number of particles per clutch was estimated from a determination of the average number of particles per compact, namely 2293 for Batch 14156 (Marshall 2019).

[b] Gray shading indicates that the water rinse was not added to the total.

[c] Individual DUF_{Pre} is the preburn leach fraction of exposed uranium in each clutch with <0.5 exposed kernel equivalents.

Table 8. Uranium leached from 25% PF compacts after the burn

Series	Clutch	Particles [a]	First leach	Second leach	H_2O rinse [b]	Total	DUF_{Post} [c]
1	14156C/D-1	11,465	1.25E-2	3.59E-4	2.04E-5	0.013	1.13E-6
	14156C/D-2	11,465	1.35E-2	2.96E-4	2.12E-5	0.014	1.20E-6
	14156C/D-3	11,465	1.29E-1	2.31E-4	1.79E-5	0.129	1.13E-5
	14156C/D-4	11,465	1.25E-2	3.94E-4	7.68E-5	0.013	1.13E-6
	14156C/D-5	11,465	1.17E+0	5.52E-3	5.42E-4	1.176	---
	14156C/D-6	11,465	2.16E+0	5.85E-3	4.08E-4	2.164	---
	14156C/D-7	11,465	1.45E-2	6.71E-4	1.01E-4	0.015	1.32E-6
	14156C/D-8	11,465	1.35E-2	2.59E-3	1.09E-4	0.016	1.40E-6
2	14156D-1	11,465	1.25E-2	4.21E-4	1.74E-5	0.013	1.12E-6
	14156D-2	11,465	1.27E-1	1.18E-1	2.92E-4	0.246	2.14E-5
	14156D-3	11,465	1.21E-2	3.05E-4	6.00E-5	0.012	1.08E-6
	14156D-4	11,465	1.25E-2	3.37E-4	3.21E-5	0.013	1.12E-6

Note: Uranium content in each leach is reported in kernel equivalents.
[a] The number of particles per clutch was estimated from a determination of the average number of particles per compact, namely 2293 for Batch 14156 (Marshall 2019).
[b] Gray shading indicates that the water rinse was not added to the total.
[c] Individual DUF_{Post} is the postburn leach fraction of exposed uranium in each clutch with <0.5 exposed kernel equivalents.

The calculated DUF_{Pre} and DUF_{Post} for clutches with <0.5 kernel equivalents of leached uranium were fairly consistent except for four significant outliers. Clutch 14156C/D-3 had elevated levels of uranium detected in both the preburn and postburn leach series, Clutch 14156C/D-4 had a slightly elevated level of uranium in the preburn leach series, and Clutch 14156D-2 had elevated levels detected in the postburn leach series. The source of these abnormally high levels of leached uranium can only be conjectured using the existing data. Possible sources may be (1) individual particles with an exposed kernel or SiC defect that were incompletely leached, or (2) the excess uranium could be from inclusion of a kernel fragment or some other localized uranium contamination. Incomplete leaching of the kernel in an individual particle due to restriction of acid infiltration to the kernel is unlikely for the preburn and postburn leaches of Clutch 14156C/D-3 because the successive analysis of the first leach, the second leach, and the water rinse showed significant reduction in the amount of uranium leached at each step, and the second postburn leach was very low, with a total of only 0.345 kernel equivalents leached. A more likely scenario is that an abnormally high amount of uranium was in the OPyC or matrix, and this uranium was in a form that was not easily leached until after the burn. Two observations support this hypothesis: (1) while the amount of uranium detected in each successive preburn leach dropped by approximately an order of magnitude, the amount in each leach was higher than observed in most of the other clutches, and (2) the amount of uranium leached after the burn dropped approximately three orders of magnitude after the first postburn leach to a level less than observed in most of the other clutches. The preburn leach progression in Clutch 14156C/D-4 also suggests localized uranium contamination in the OPyC or matrix. In contrast, the elevated amount of uranium detected in the postburn leaches of Clutch 14156D-2 appears to be more consistent with incomplete leaching of the kernel from a particle with defective SiC because the second acid leach contained almost as much uranium as the first.

After LBL, all particles in Clutch 14156D-2 were mounted in a single layer on Kapton tape for x-ray radiography. Examination of the x-ray radiographs revealed one particle with unusual x-ray opacity. This particle is shown in Figure 3a, where the darker areas in the radiograph indicate lower x-ray attenuation and the brighter areas indicate higher x-ray attenuation. The abnormal particle was removed from the

Kapton tape and imaged with x-ray computed tomography (XCT). The x-ray tomogram in Figure 3b shows a lining inside the SiC layer containing material with high atomic number (Z), probably uranium. The interior of the particle could not be imaged because of the x-ray attenuation in this high-Z lining. A region of degraded SiC can also be seen in Figure 3b, with high-Z material in the degraded region. It is possible that some of the particle's uranium was leached through the region of degraded SiC and that this particle is responsible for most of the 0.246 kernel equivalents detected during the postburn leach of Clutch 14156D-2. Confirmation of this hypothesis would require further analysis to determine how much uranium remains in the particle and why the SiC degradation only resulted in partial leaching.

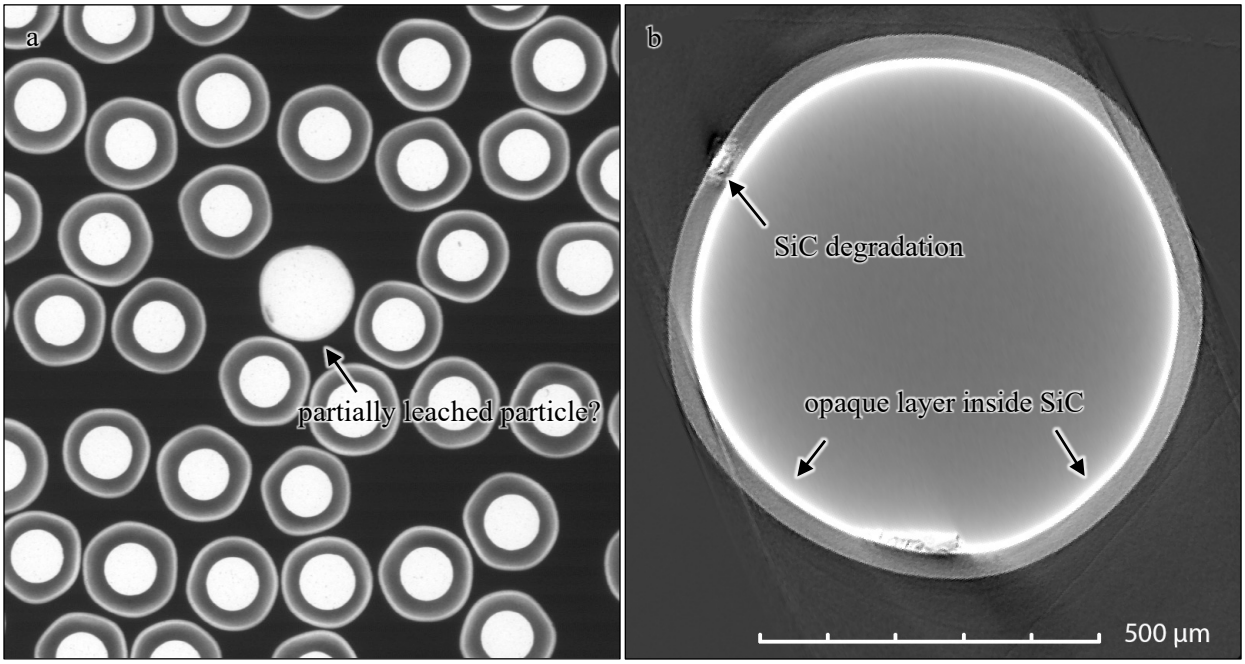

Figure 3. (a) Low resolution x-ray radiograph and (b) high-resolution x-ray tomogram showing what may be a partially leached particle from Clutch 14156D-2.

Table 9 shows the DUF data for the 25% PF compacts in terms of mean, standard deviation, and upper bounds of the 95% confidence interval of the mean value for the sampled material based on the measured samples. The distributions of the DUF values determined by the LBL analysis of the 25% PF compacts suggest that the measured DUF is comprised of uniformly distributed dispersed uranium plus localized higher concentrations in a few individual compacts. Such outliers do not conform to the definition for dispersed uranium and the assumption that it is a variable property as measured. Table 9 shows the calculated DUF using all available data and two alternate calculations using filtered data sets, where outliers were excluded to estimate the uniformly distributed contribution. Filtering was achieved by first calculating the median and median absolute deviation (MAD) from all available DUF_{Pre} and DUF_{Post} values, and then excluding values that deviated from the median by more than selected multiples of the MAD. A filter criterion of <10×MAD above the median can be considered to be a conservative approach for culling out only the outliers with an extreme deviation, and it resulted in the filtering out of the DUF contributions from the Clutch 14156C/D-3 preburn leach, the Clutch 14156C/D-3 postburn leach, and the Clutch 14156D-2 postburn leach. A filter criterion of <3×MAD above the median also filtered out the Clutch 14156C/D-4 preburn leach data. The mean, standard deviation, and 95% confidence limit for the filtered DUF values shown in Table 9 were calculated with the standard methods prescribed in the AGR-5/6/7 Fuel Specification and discussed in ORNL/TM-2019/1154 (Hunn et al. 2019).

Table 9. Dispersed uranium in 25% PF compacts

		DUF_{Pre}	DUF_{Post}	DUF_{Total}
All data	Measured mean	5.20E-6	4.22E-6	9.42E-6
	Standard deviation	4.63E-6	6.83E-6	---
	95% confidence limit	≤ 7.73E-6	≤ 8.19E-6	≤ 1.42E-5
All data	Measured median	3.79E-6	1.17E-6	---
	Median absolute deviation	7.30E-7	6.48E-8	---
<10×MAD filtered data [a]	Measured mean	3.83E-6	1.19E-6	5.02E-6
	Standard deviation	1.12E-6	1.14E-7	---
	95% confidence limit	≤ 4.49E-6	≤ 1.27E-6	≤ 5.68E-6
<3×MAD filtered data [b]	Measured mean	3.53E-6	1.19E-6	4.72E-6
	Standard deviation	5.87E-7	1.14E-7	---
	95% confidence limit	≤ 3.90E-6	≤ 1.27E-6	≤ 5.10E-6

[a] The <10×MAD filtered data do not include data from the Clutch 14156C/D-3 preburn leach, the Clutch 14156C/D-3 postburn leach, or the Clutch 14156D-2 postburn leach.
[b] The <3×MAD filtered data do not include data from the Clutch 14156C/D-3 preburn leach, the Clutch 14156C/D-3 postburn leach, the Clutch 14156D-2 postburn leach, or the Clutch 14156C/D-4 preburn leach.

The DUF_{Total} mean and 95% confidence limit values for the 25% PF compact filtered data shown in Table 9 compare well with the DUF_{Total} mean value of 5.28E-6 and 95% confidence limit value of ≤5.40E-6 for the pooled OC TRISO data summarized in Table 4. This shows that the uranium contamination was generally not any higher in the majority of the 25% PF compacts than in the particles.[a] However, for cases in which the DUF_{Pre} was ~96% of the DUF_{Total} in the OC TRISO, the filtered DUF_{Pre} was ~75–76% of the DUF_{Total} in the 25% PF compacts. This could indicate that the 1,800°C heat treatment was driving reaction of the dispersed uranium with the surrounding carbon, such that the preburn leachability of the uranium was reduced. Such an effect would also explain the slow preburn leaching of what is presumed to be localized uranium contamination in Clutch 14156C/D-3.

Although the DUF_{Total} for the filtered data sets indicates that the uniformly distributed dispersed uranium was below the specified limit of ≤1E-5 at 95% confidence, the impact of the outlier data on the overall amount of exposed uranium cannot be ignored. Without supplemental analyses to show that the excess uranium leached from these outlier samples came from individual particles with exposed kernel defects or SiC defects, the most conservative approach is to include the outlier data in the calculation of mean DUF because the specification on maximum DUF is the most stringent (≤1E-5 at 95%) compared to the limits on EKF (≤5E-5 at 95%) and SDF (≤1E-4 at 95%). The upper bounds of the 95% confidence interval of the mean value for the sampled material—based on the DUF_{Total} calculated without filtering the outlier DUF data—are above the AGR-5/6/7 specified limit of ≤1E-5 at 95% confidence. Thus, it appears that the cause of the 25% PF compact batches failing to meet the specified criteria for DUF_{Total} may be associated with abnormal, localized contamination in individual compacts (most likely in individual particles). In addition, the fact that the outlier DUF values skewed the distribution of measured

[a] While the data in Table 4 are from OC TRISO used for the 40% PF compacts, it is reasonable to presume that the source of the DUF, EKF, and SDF is from the underlying TRISO particles that were used for both AGR-5/6/7 packing fractions. Therefore, comparisons between the 40% PF OC TRISO and the 25% PF compacts are valid.

DUF values suggests that the t-test based on means and standard deviations may not be appropriate for the calculation of the confidence interval.

Table 10 shows the calculated EKF and SDF for the 25% PF compacts. The 95% confidence limits in the table correspond to the true defect fractions in the sampled population that yield a cumulative binomial distribution value of 0.95 for the observed number of defects and sample size. These values are the lowest tolerance limits for which the compact lot would be deemed acceptable at 95% confidence based on the sample measured. The 95% confidence upper limits for EKF and SDF calculated from the pooled data were below the AGR-5/6/7 specified maximum values for EKF (≤5E-5 at 95%) and SDF (≤1E-4 at 95%). In the previous analysis of the first test series of 40 25% PF compacts that was reported in ORNL/TM-2018/744, the 95% confidence upper limit on EKF (≤5.18E-5) was just above the specified maximum. It was hypothesized in that report that additional sampling of the 25% PF compacts would likely provide a lower 95% confidence limit because the measured defect fraction in the 40-compact sample was only 1.09E-5. This hypothesis has been confirmed via the addition of 20 more compacts to the sample size.

Table 10. Defect fractions in 25% PF compacts

	EKF	SDF
Number of defects	1	3
Number of particles	~137,580	~137,580
Measured defect fraction	7.27E-6	2.18E-5
95% confidence limit	≤ 3.45E-5	≤ 5.64E-5

The measured defect fractions for EKF and SDF obtained from the 60 analyzed 25% PF compacts (Table 10) were higher than the measured defect fractions for EKF and SDF obtained from the OC TRISO analysis but were less than the 95% confidence limits for the OC TRISO EKF and SDF (Table 5). Comparison suggests that the 25% PF compacting may have resulted in a minor increase in the defect fractions, but the statistics do not provide significant certainty for this conclusion. Any increase can be considered essentially insignificant compared to the AGR-5/6/7 fuel specification limits given that the 25% PF compacts nevertheless pass the acceptance tests for EKF and SDF based on the data in Table 10. As discussed below, there is much stronger evidence that increasing the packing fraction to 40% resulted in significant particle damage. Therefore, it is possible that some particle damage was also occurring during compacting of the 25% PF compacts, but with lower probability due to the lower packing fraction.

2.1.1.1.3 Results for 40% PF Compacts

Table 11 shows the amounts of uranium (in kernel equivalents) detected in the solutions collected during preburn leaching of the 40% PF compact clutches, and Table 12 shows similar data for the postburn leaching. Individual preburn leach DUF_{Pre} values and postburn leach DUF_{Post} values are shown for cases in which the total uranium leached before or after the burn was <0.5 kernel equivalents, respectively. There was a significant amount of uranium in each of the preburn leach water rinse solutions for the first four samples in the first test series (>10% of the second leach and >1% of the average uranium per kernel), so these data were included in the total leached uranium values. The water rinses were not analyzed for the other samples in the first test series.

Similar to what was observed in the 25% PF compact analysis, the calculated DUF_{Pre} and DUF_{Post} values for individual clutches were fairly consistent except for two significant outliers in the preburn leach of Clutch 14155C-2 and the postburn leach of Clutch 14154C-3. Table 13 shows the DUF results based on all available DUF data in Table 11 and Table 12 vs. a reduced data set in which these two

outliers were excluded using a filter criteria of <10×MAD on the pooled data as described above. As for the 25% PF compacts, the outlier contribution to the DUF_{Total} measured for the 40% PF compacts resulted in an upper bound on the 95% confidence interval of the mean value for the sampled compacts that was slightly above the AGR-5/6/7 specified limit of ≤1E-5.

Table 11. Uranium leached from 40% PF compacts before the burn

Series	Clutch	Particles [a]	First leach	Second leach	H_2O rinse [b]	Total	DUF_{Pre} [c]
1	14154C-1	~17,395	1.95E+0	1.38E-1	3.03E-2	2.12	---
	14154C-2	~17,395	8.55E-1	1.89E+0	3.22E-1	3.07	---
	14154C-3	~17,395	1.82E+0	1.86E-1	3.79E-2	2.04	---
	14154C-4	~17,395	2.47E+0	2.43E-1	2.79E-2	2.75	---
	14154C-5	~17,395	2.76E-2	5.73E-3		0.03	1.91E-6
	14154C-6	~17,395	3.87E-2	6.84E-3		0.05	2.62E-6
	14154C-7	~17,395	9.33E-1	1.52E-1		1.09	---
	14154C-8	~17,395	2.60E-2	6.36E-3		0.03	1.86E-6
2	14154C-1	~17,395	1.03E+0	3.71E-3	1.22E-4	1.03	---
	14154C-2	~17,395	9.75E-1	4.78E-2	8.33E-4	1.02	---
	14154C-3	~17,395	1.02E+0	4.72E-2	1.38E-3	1.07	---
	14154C-4	~17,395	3.11E-2	5.01E-3	1.68E-4	0.04	2.08E-6
	14155C-1	~17,100	4.23E+0	2.34E-1	7.36E-3	4.46	---
	14155C-2	~17,100	2.02E-1	2.65E-2	1.07E-3	0.23	1.33E-5
	14155C-3	~17,100	4.14E-2	5.03E-3	2.78E-4	0.05	2.71E-6
	14155C-4	~17,100	1.97E+0	1.01E-1	3.60E-3	2.08	---
	14155C-5	~17,100	1.91E+0	8.33E-2	2.50E-3	1.99	---
	14155C-6	~17,100	3.90E-2	3.92E-3	2.80E-4	0.04	2.51E-6
	14155C-7	~17,100	1.98E+0	1.35E-1	5.23E-3	2.12	---
	14155C-8	~17,100	9.98E-1	5.82E-2	2.60E-3	1.06	---

Note: Uranium content in each leach is reported in kernel equivalents.

[a] The number of particles per clutch was estimated from a determination of the average number of particles per compact, namely 3479 for Batch 14154 and 3420 for Batch 14155 (Marshall 2019).

[b] Gray shading indicates that the water rinse was not added to the total; blanks indicate that no measurement was taken.

[c] Individual DUF_{Pre} is the preburn leach fraction of exposed uranium in each clutch with <0.5 exposed kernel equivalents.

Table 12. Uranium leached from 40% PF compacts after the burn

Series	Clutch	Particles [a]	First leach	Second leach	H_2O rinse [b]	Total	DUF_{Post} [c]
1	14154C-1	~17,395	1.03E+0	8.35E-3	1.38E-4	1.04	---
	14154C-2	~17,395	8.10E-2	5.14E-3	2.10E-4	0.09	4.95E-6
	14154C-3	~17,395	8.27E-1	1.23E-2	2.44E-4	0.84	---
	14154C-4	~17,395	7.23E-1	3.17E-1	3.70E-3	1.04	---
	14154C-5	~17,395	3.70E-2	7.26E-4	8.88E-5	0.04	2.17E-6
	14154C-6	~17,395	3.14E-2	7.58E-4	1.50E-4	0.03	1.85E-6
	14154C-7	~17,395	1.06E+0	8.41E-3	1.60E-4	1.07	---
	14154C-8	~17,395	3.47E-2	6.62E-4	2.03E-4	0.04	2.03E-6
2	14154C-1	~17,395	4.09E-2	1.94E-2	1.68E-3	0.06	3.47E-6
	14154C-2	~17,395	2.07E+0	1.20E-2	1.86E-3	2.08	---
	14154C-3	~17,395	7.98E-2	3.18E-2	4.43E-4	0.11	6.42E-6
	14154C-4	~17,395	2.07E+0	3.91E-2	2.11E-4	2.11	---
	14155C-1	~17,100	1.13E+0	3.28E-3	2.44E-4	1.13	---
	14155C-2	~17,100	1.14E+0	4.28E-3	4.20E-4	1.15	---
	14155C-3	~17,100	2.85E+0	4.19E-3	1.93E-4	2.85	---
	14155C-4	~17,100	3.83E-2	2.45E-4	2.27E-4	0.04	2.25E-6
	14155C-5	~17,100	1.10E+0	4.53E-3	4.04E-5	1.10	---
	14155C-6	~17,100	3.23E-2	9.55E-4	1.07E-5	0.03	1.94E-6
	14155C-7	~17,100	1.03E+0	5.11E-3	6.40E-5	1.03	---
	14155C-8	~17,100	1.04E+0	4.89E-3	1.16E-4	1.04	---

Note: Uranium content in each leach is reported in kernel equivalents.
[a] The number of particles per clutch was estimated from a determination of the average number of particles per compact, namely 3479 for Batch 14154 and 3420 for Batch 14155 (Marshall 2019).
[b] Gray shading indicates that the water rinse was not added to the total.
[c] Individual DUF_{Post} is the postburn leach fraction of exposed uranium in each clutch with <0.5 exposed kernel equivalents.

Table 13. Dispersed uranium in 40% PF compacts

		DUF_{Pre}	DUF_{Post}	DUF_{Total}
All data	Measured mean	3.86E-6	3.14E-6	7.00E-6
	Standard deviation	4.19E-6	1.70E-6	---
	95% confidence limit	≤ 6.95E-6	≤ 4.28E-6	≤ 1.04E-5
All data	Measured median	2.51E-6	2.21E-6	---
	Median absolute deviation	4.30E-7	3.13E-7	---
<10×MAD filtered data [a]	Measured mean	2.28E-6	2.67E-6	4.95E-6
	Standard deviation	3.75E-7	1.15E-6	---
	95% confidence limit	≤ 2.60E-6	≤ 3.51E-6	≤ 5.86E-6

[a] The <10×MAD filtered data do not include 14155C-2 preburn and 14154C-3 postburn data.

The measured mean DUF_{Total} for the <10×MAD filtered data set from the 40% PF compact analysis (4.95E-6) compares well with the measured mean DUF_{Total} values for the OC TRISO pooled sample reported in Table 4 (5.28E-6) and the <10×MAD filtered data set from the 25% PF compact sample reported in Table 9 (5.02E-6). This further reinforces the conclusions that there was a component of the total DUF uniformly distributed throughout the compacts and that this component was no higher than what was in the particles used to make the compacts. As observed when comparing the OC TRISO to the 25% PF compacts, the leachability of the uniformly dispersed uranium appeared different in the 40% PF compacts, presumably because of the thermal treatment of the compacts during processing. In the 40% PF compacts, ~46% of the <10×MAD filtered DUF was detected in the preburn leach compared to ~96% in the OC TRISO.

Table 14 shows the calculated EKF and SDF for the 40% PF compacts based on the data in Table 11 and Table 12. The 95% confidence limits in the table correspond to the true defect fractions in the sampled population that yield a cumulative binomial distribution value of 0.95 for the observed number of defects and sample size. These values are the lowest tolerance limits for which the compact lot would be deemed acceptable at 95% confidence based on the sample that was measured. Results are provided for Batches 14154C and 14155C separately and as a pooled data set. While the defect fractions in Batch 14155C may be marginally higher than those in Batch 14154C, the statistics indicate that the difference is not likely to be significant with respect to the measured defect fractions. Pooling the data should not skew the data analyses more than ~1E-5, and it is statistically favorable to pool the data to reduce the uncertainty associated with the sample sizes. The SDF data for Batch 14154C indicate that the sampled population satisfied the specified limit of SDF ≤ 1E-4 at 95% confidence, as did the pooled population. The available SDF data for Batch 14155C was insufficient to show that the sampled population satisfied the specification, although it would pass a specified limit of SDF ≤ 1E-4 with 93.7% confidence, and additional sampling would most likely result in a positive acceptance test. Both individual batches and the pooled population failed to meet the specification of EKF ≤ 5E-5 at 95% confidence, and there is no indication that additional sampling would change this rejection result, given that the measured EKF values were all higher than the specified limit.

Table 14. Defect fractions in 40% PF compacts

Batch		EKF	SDF
14154C	Number of defects	14	8
	Number of particles	~208,740	~208,740
	Measured defect fraction	6.71E-5	3.83E-5
	95% confidence limit	≤ 1.05E-4	≤ 6.92E-5
14155C	Number of defects	11	8
	Number of particles	~136,800	~136,800
	Measured defect fraction	8.04E-5	5.85E-5
	95% confidence limit	≤ 1.34E-4	≤ 1.06E-4
Pooled	Number of defects	25	16
	Number of particles	~345,540	~345,540
	Measured defect fraction	7.24E-5	4.63E-5
	95% confidence limit	≤ 1.02E-4	≤ 7.04E-5

The measured defect fractions for EKF and SDF reported in Table 14 for the individual batches and the pooled sample of 100 analyzed 40% PF compacts are higher than the EKF and SDF reported in Table

5 for the OC TRISO. There is strong evidence that the EKF in the pooled population of 40% PF compacts was higher than the EKF in the pooled population of OC TRISO, which indicates that the 40% PF compacting process was damaging the TRISO coatings, and kernels were exposed. There was also a less dramatic increase in SDF, indicating that the SiC layers in some particles were broken, but at least one of the pyrocarbon coatings remained liquid tight until after the burn.

Table 11 shows the preburn leach results for the eight compact clutches in the first test series. There were ten exposed kernels in the first group of four compacts and only one in the second group. This result is discussed in ORNL/TM-2018/744 (Hunn et al. 2018) as an unlikely distribution if the failure mechanism were dependent on a particle attribute and only an ~10% probable distribution if the failure mechanism was dependent on variability in processing between individual compacts. This raised questions regarding the possibility of the observed particle defects being an artifact of the LBL performed on the first group in the first test series and it was recommended in ORNL/TM-2018/744 that additional samples be analyzed to determine if the improbable distribution was real or if it was an artifact of the LBL process. The number and distribution of exposed kernels in the preburn leach analysis of the second test series of 60 additional 40% PF compacts provides evidence that the EKF determined from the 40 compacts in the first test series was accurate and does not support a conclusion that the 10 defects measured in the first group represent an LBL artifact. In fact, the measured EKF from the first test series reported in ORNL/TM-2018/744 (7.90E-5) is nearly the same as the results for the pooled data reported in Table 14.

2.1.1.1.4 Conclusions from ORNL LBL Analysis of AGR-5/6/7 Compacts

LBL analysis was completed on 100 40% PF compacts and 60 25% PF compacts taken from compact batches used for the AGR-5/6/7 irradiation test. Additional LBL was performed on OC TRISO taken from the composite used to form the 40% PF compacts to explore whether overcoating or compacting was responsible for the elevated EKF observed in the 40% PF compacts. Results of these analyses, as well as additional analysis and comparison to LBL analysis performed at BWXT NOG were reported in ORNL/TM-2019/1154 (Hunn et al. 2019).

The LBL analysis of the OC TRISO showed that overcoating did not introduce significant damage to the TRISO particles. Statistical comparison of the EKF and SDF in the OC TRISO samples with the EKF and SDF in the TRISO samples showed similar defect fractions in the sampled populations. The OC TRISO LBL analysis also provided evidence that the DUF was a combination of uniformly distributed uranium contamination combined with high concentrations of uranium in some of the compacts. Although this localized contamination complicated the analysis, consistency was observed between the DUF in the OC TRISO and the DUF in the two types of compacts. Comparison to the TRISO particles was limited by the available data, but it is probable that uranium contamination in the TRISO particles was the source of all observed DUF.

While there was some variation in the observed EKF for the analyzed samples of TRISO, OC TRISO, and 25% PF compacts, there were no strong indications for significant statistical differences after accounting for the sample sizes. The TRISO, OC TRISO, and 25% PF compacts were all found to have acceptable values for EKF compared to the AGR-5/6/7 specified limit of EKF ≤ 5E-5 at 95% confidence. However, the EKF for the 40% PF compacts clearly indicated that TRISO particles were damaged during compacting, and the 40% PF compacts did not satisfy the specification limit on EKF.

The ORNL SDF data indicated that no significant damage was introduced in the SiC layer during compacting of the 25% PF compacts. However, for the 40% PF compacts, the SDF was slightly higher than the OC TRISO and 25% PF compacts, which suggests that the SiC layers in some particles were broken by the 40% PF compacting process but at least one of the pyrocarbon coatings remained liquid tight until after the burn. Nevertheless, the pooled SDF for the 40% PF compacts indicated they satisfied the specified limit of SDF ≤ 1E-4 at 95% confidence.

2.1.1.1.5 References

Helmreich, G. W., J. D. Hunn, D. J. Skitt, J. A. Dyer, and A. T. Schumacher. 2017a. *Acceptance Test Data for the AGR-5/6/7 Irradiation Test Fuel Composite—Defective IPyC and Pyrocarbon Anisotropy*. ORNL/TM-2017/037. Oak Ridge, Tennessee: Oak Ridge National Laboratory.

Helmreich, G. W., J. D. Hunn, D. J. Skitt, J. A. Dyer, and A. T. Schumacher. 2017b. *x-ray Analysis of Defects and Anomalies in AGR-5/6/7 TRISO Particles*. ORNL/TM-2017/038. Oak Ridge, Tennessee: Oak Ridge National Laboratory.

Hunn, J. D., F. C. Montgomery, J. A. Dyer, T. J. Keever, and G. W. Helmreich. 2018. *Confirmatory LBL Analysis of AGR-5/6/7 Compacts and Overcoated Particles.* ORNL/TM-2018/774. Oak Ridge, Tennessee: Oak Ridge National Laboratory.

Hunn, J. D., F. C. Montgomery, G. W. Helmreich, A. K. Kercher. 2019. *Additional Confirmatory LBL Analysis of AGR-5/6/7 Compacts and Overcoated Particles.* ORNL/TM-2019/1154. Oak Ridge, Tennessee: Oak Ridge National Laboratory.

Marshall, D. W. 2018. *Confirmatory Defect Analyses of AGR-5/6/7 Fuel.* INL/EXT-18-45110, Revision 0. Idaho Falls, Idaho: Idaho National Laboratory.

Marshall, D. W. 2019. "Fuel Summary." Personal communication by e-mail on April 16, 2019 with an attached spreadsheet that was used for INL/EXT-18-45110, Revision 0 (Marshall 2018).

2.1.2 Safety-Testing and Post-Irradiation Examination

2.1.2.1 Oxidation of Matrix Material in Helium with Varied Moisture Content

HTGRs traditionally use TRISO-coated particle fuel compacted in a graphite and carbonized resin matrix to produce a fuel element. Accident scenarios in HTGRs include air and moisture ingress events at high temperatures. The likelihood of such accidents may vary among HTGR designs. Exploration of the oxidation behavior of matrix material from TRISO-coated particle fuel elements in moisture environments provides critical data needed to predict the material's response during off-normal accident scenarios. The US DOE AGR initiated an experimental effort to better understand the oxidation response of each component in such events. By testing each component (matrix-only or TRISO particles) separately, the oxidation behavior can be isolated, measured, and subsequently leveraged in fuel performance models to better predict performance.

Near-representative, matrix-only samples were fabricated to facilitate oxidation testing in varied moisture concentrations. Fabrication of matrix-only samples and early oxidation test results were summarized in a previous quarterly report (INL/EXT-18-44496, October, November, December 2017). Oxidation testing has now been completed over a range of temperatures and oxidizing environments to obtain relevant oxidation kinetics parameters and empirical oxidation rates. The acquired oxidation rates were fit to established models for steam oxidation of nuclear graphite, and data were acquired following an established process. The data showed good agreement over conditions typical of the kinetic regime, and they showed a departure from the kinetic model fit at elevated temperatures and steam partial pressures in helium carrier gas. The departure was confirmed to be due to the experimental conditions being beyond the kinetic regime based on destructive analysis. A comprehensive report on this matrix oxidation study (ORNL/TM-2019/1341) was issued in November 2019 (Gerczak et al. 2019) and excerpts have been extracted from this report to provide the summary presented herein.

2.1.2.1.1 Testing Approach

The oxidation behavior for different grades of nuclear-grade graphite in steam conditions relevant to chronic oxidation of HTGR internal components has been well established (Velasquez, Hightower, and Burnette 1978; Overholser and Blakely 1965; Contescu et al. 2014). However, the oxidation behavior of the matrix material in steam environments has not been well studied. Additionally, the matrix material is a

composite of natural and synthetic graphite flake and carbonized resin binder, so existing data on nuclear graphite stream oxidation may not translate directly. Therefore, there is a need to directly analyze the oxidation performance of representative matrix material. Two testing approaches were employed in this effort. One focused on acquiring the kinetic parameters for steam oxidation of near-representative matrix-only material. The other focused on obtaining empirical oxidation rates at conditions relevant to accident scenarios.

In 2012, an effort at ORNL to measure the steam oxidation kinetics of various nuclear-grade graphites was initiated (Contescu, Burchell, and Mee 2013; Contescu et al. 2014; Contescu, Burchell, and Mee 2015; Contescu, Lee, and Mee 2018; Contescu and Mee 2018). This past effort served as a template for the oxidation kinetics study of matrix-only material in varied moisture environments, and it included measured oxidation rates under various partial pressures of water (P_{H2O}) and hydrogen (P_{H2}). Hydrogen was included as hydrogen will suppress the reaction by occupying surface sites on the graphite (Giberson and Walker 1966; Contescu et al. 2018). Therefore, the influence of the partial pressure of hydrogen must be considered when analyzing the oxidation behavior in a steam environment. This testing approach focused on determining the relevant kinetic parameters based on an established model, the Langmuir-Hinshelwood (LH) model (Walker, Rusinko, and Austin 1959), and on a new model, the Boltzmann-enhanced Langmuir-Hinshelwood (BLH) model, which accounts for the temperature dependence of the reaction order (Hurt and Calo 2001). The test matrices from these previous studies for steam and hydrogen in ultra-high purity helium were used as a guide for the matrix-only sample test matrix (Table 15). A dual symmetrical thermogravimetric analyzer (TAG) 16/18 (Setaram, France) was used to measure the oxidation rates.

Table 15. Test matrix for oxidation kinetics evaluation in varied moisture environments

		P_{H2O} (Pa)					
		20	100	200	300	500	1000
P_{H2} (Pa)	0 [a]	✓	✓	✓	✓	✓	✓
	25	✓	✓	✓	✓	✓	
	100	✓	✓	✓	✓	✓	

[a] The P_{H2} = 0 conditions were tested twice.

The oxidation behavior at near-accident conditions was pursued to obtain empirical rates so that oxidation behavior at extreme conditions could be predicted better, and the nature of the oxidation response could be better understood. An existing high temperature steam exposure system, the High Temperature Module (HTM) of the Severe Accident Test Station, was leveraged to study this behavior, as described by Gerczak et al. (2019). This system limited the conditions which could be obtained because the system operated at nominally atmospheric pressure.

Table 16. Test matrix for high temperature steam oxidation tests

		Steam temperature			
		1,200 °C	1,300 °C	1,400 °C	1,500 °C
P_{H2O} (kPa)	0 [a]	✓	✓	✓	✓
	10	✓	✓	✓	✓
	20	✓	✓	✓	
	30	✓	✓	✓	
	48	✓			

[a] The P_{H20} = 0 conditions were to determine contribution from residual oxygen.

2.1.2.1.2 Oxidation Kinetics Testing

A total of 184 rate values were measured at the various temperatures and gas compositions defining the test matrix. The kinetic parameters were determined following the same process used to determine kinetic parameters for the LH and BLH models for nuclear-grade graphite, and the following description of the data analysis approach is mostly reproduced from a technical report by Contescu, Lee, and Mee (2018).

To measure the kinetic parameters for LH and BLH models, all valid data were simultaneously analyzed by solving a set of multiple nonlinear rate equations based on the global oxidation reaction, from which the most probable parameter values were found by minimization of the sum of squared errors for Y = log (*Rate*), where Y is the rate measured at any given condition, and *Rate* is the weight-normalized oxidation rate ($mg_{oxidized}$ / $mg_{initial}$/ s). Two different rate equations based on the global equation for graphite oxidation in steam (Contescu, Lee, and Mee 2018) were used for data analysis of the LH and BLH models:

For the LH model, the rate equation was

$$Rate_{LH}(P_{H2O}P_{H2},T) = \frac{k_1 P_{H2O}}{1+k_2(P_{H2})^{0.5}+k_3 P_{H2O}}, \quad (1)$$

with

$$k_i = A_i exp\left(-\frac{E_i}{RT}\right). \quad (2)$$

In these equations, T is the temperature in K, E is the activation energy in J·mol^{-1}, k_i represents the three rate constants (for i = 1, 2, and 3), and R is the gas constant (8.314 J·mol^{-1}·K^{-1}). This kinetic model has six parameters which must be estimated by fitting all data: three pre-exponential factors (A_i) and three apparent activation energies (E_i).

For the BLH model, the rate equation was

$$Rate_{BLH}(P_{H2O}P_{H2},T) = \frac{k_1(P_{H2O})^{m(T)}}{1+k_2(P_{H2})^{0.5}+k_3(P_{H2O})^{m(T)}}, \quad (3)$$

with

$$k_i = A_i exp\left(-\frac{E_i}{RT}\right) \quad (4)$$

and

$$m(T) = m_{max} + \frac{m_{min}-m_{max}}{1+exp\left(\frac{T-T_0}{\theta}\right)}. \quad (5)$$

The BLH kinetic model was developed to account for the faster increase of oxidation rates at water vapor pressures >100 Pa and temperatures >950°C, relative to that predicted by the LH model. Such differences between the experimental rates and those predicted by the LH model were observed in prior studies of medium-grain graphites (PCEA and NBG-17), and superfine grain graphites (IG-110 and 2114) in a similar range of oxidant pressures and temperatures (Contescu, Lee, and Mee 2018; Contescu et al. 2018). The BLH model was introduced to represent the data with a unique, more robust model. The BLH model accounts for an increased rate by introducing a correction to the LH model, assuming that the reaction order for the oxidant depends on temperature. This dependence, *m(T)*, was best modeled by the integral Boltzmann distribution function with four new parameters: T_0, m_{min}, m_{max}, and θ (Equation 5). The values of m_{min} and m_{max} define the range of apparent reaction order. The characteristic temperature (T_0) is associated with the inflection of the *m(T)* function, and the value θ is a scaling parameter equal to the inverse slope of *m(T)* at T_0. With these changes, the BLH model has ten parameters that must be estimated from the collected data.

The rate data over the range of analyzed conditions (P_{H2O}, P_{H2}, T) were fit to the analytical solutions in Equation 6 and Equation 7 for the LH and BLH models, respectively. Equation 6 and Equation 7 were obtained by combining the equations which describe the LH (Equation 1 and Equation 2) and BLH (Equation 3–Equation 5) models, respectively. From these fits, the pre-exponential factors (A_i) and apparent activation energies (E_i) for each term were obtained, along with the apparent reaction order ($m(T)$). Figure 4 shows the LH and BLH fits to the experimental oxidation rate data for 16 Pa < P_{H2O} < 688 Pa, P_{H2} = 0, and 850 °C < T < 1,200°C, where the individual data points represent the measured data and the isotherms represent the fits to the analytical solutions.

$$Rate_{LH}(P_{H2O}P_{H2},T) = \frac{A_1 exp\left(-\frac{E_1}{RT}\right)(P_{H2O})}{1+A_2 exp\left(-\frac{E_2}{RT}\right)(P_{H2})^{0.5}+A_3 exp\left(-\frac{E_3}{RT}\right)(P_{H2O})} \quad (6)$$

$$Rate_{BLH}(P_{H2O}P_{H2},T) = \frac{A_1 exp\left(-\frac{E_1}{RT}\right)(P_{H2O})^{\left[m_{max}+\frac{m_{min}-m_{max}}{1+exp\left(\frac{T-T_o}{\theta}\right)}\right]}}{1+A_2 exp\left(-\frac{E_2}{RT}\right)(P_{H2})^{0.5}+A_3 exp\left(-\frac{E_3}{RT}\right)(P_{H2O})^{\left[m_{max}+\frac{m_{min}-m_{max}}{1+exp\left(\frac{T-T_o}{\theta}\right)}\right]}} \quad (7)$$

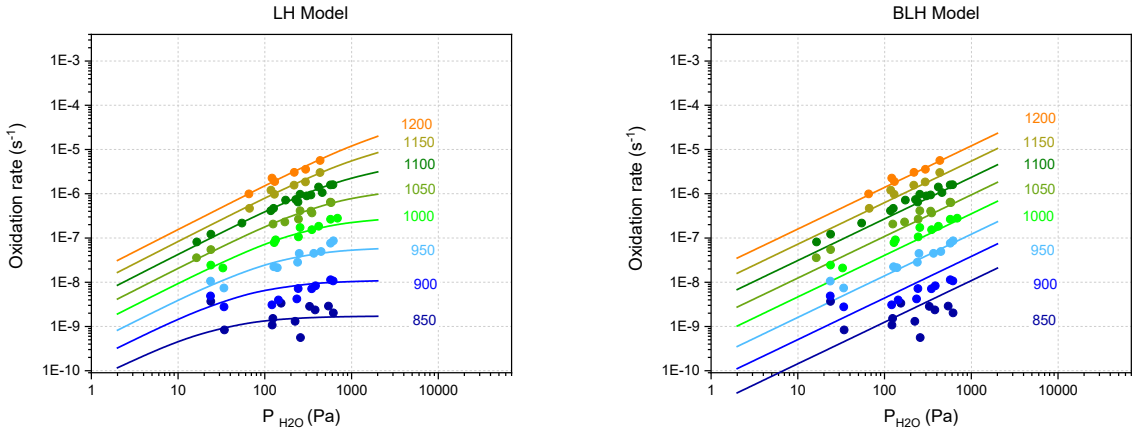

Figure 4. Experimental oxidations rates at P_{H2} = 0 with isothermal trend lines reflecting kinetic parameters determined from best fit for LH and BLH models.

The parameters for both the LH and BLH models are listed in Table 17. Comparison of the isothermal trend lines in Figure 4 suggests that at temperatures above 950°C and pressures above P_{H2O} > 200 Pa, the BLH model better represents the data, while at lower temperatures and pressures, the LH model better represents the data. This was previously suggested for nuclear-grade graphite, but the variation at higher temperatures and pressures was more pronounced than that suggested in this data set (Contescu et al. 2018).

Table 17. Experimentally determined kinetic parameters for LH and BLH models

LH model		BLH model			
A_1	2.8E-2 $(Pa)^{-1}$	A_1	1.1E+2 $(Pa \cdot s)^{-m}$	m_{max}	0.94
A_2	4.0E-10 $(Pa)^{-0.5}$	A_2	6.6E-5 $(Pa)^{-0.5}$	m_{min}	0.11
A_3	2.1E-16 $(Pa)^{-1}$	A_3	3.4E-4 $(Pa)^{-m}$	T_o	1146 K
E_1	181 kJ/mol	E_1	276 kJ/mol	θ	75 K
E_2	-223 kJ/mol	E_2	-87 kJ/mol		
E_3	-318 kJ/mol	E_3	42 kJ/mol		

The quality of fit for the LH and BLH models is shown in Figure 5. The double logarithmic plot compares the observed rate to the predicted rate for the same test conditions for both oxidation tests with H_2 present (red circles) and without H_2 present (blue circles). The quality of fit is represented by the correlation coefficient (R^2) for the linear fit of the data. Perfect agreement follows a linear relationship with $R^2 = 1.0$. The R^2 value for the LH fit was 0.98, and for the BLH fit it was 0.97. This indicates both models represent the data accurately over the range of conditions studied. The suggestion that the BLH model represents the data better at higher temperatures and higher pressures is indicated by the quality of fit at the higher rates (> 1E-7) compared to the lower rates (< 1E-7). Less scatter is observed at the higher rates, which are associated with higher temperatures and pressures, while more scatter is observed at the lower rates, which are associated with lower temperatures and pressures. There is less scatter in the data at the lower rates (< 1E-7) for the LH model than for the BLH model. This suggests that the LH model is a better representation of low P_{H2O} and low T, while the BLH model is a better representation at high P_{H2O} and high T.

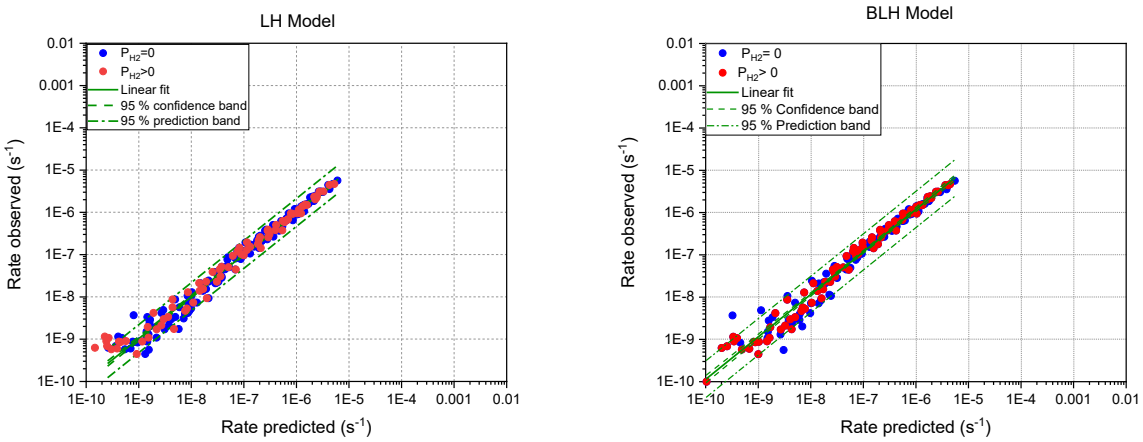

Figure 5. Observed vs. predicted rates for measured oxidation data for the LH and BLH models.

2.1.2.1.3 High-Temperature Empirical Oxidation Testing

Multiple time intervals were run for each test condition listed in Table 16 with a new sample for each run. The normalized weight loss was calculated from the difference in weight pre- and post-oxidation, divided by the pre-oxidation weight. The contribution to weight loss from residual oxygen in the system was determined by applying a linear fit to the baseline ($P_{H20} = 0$ kPa) tests for each of the temperatures of interest. This linear relationship was used to determine the normalized weight loss at equivalent exposure conditions for $P_{H20} = 10–48$ kPa. The weight-normalized contribution to weight loss from the residual oxygen calculated from the linear fit was subtracted from the measured weight loss for the oxidized samples at equivalent exposure conditions to obtain an adjusted weight loss for each condition. The weight-normalized oxidation rate (s^{-1}) was determined for each condition by a linear fit of the adjusted weight loss for each condition at a specific temperature and P_{H20}, where the slope of the fit was the rate in reciprocal seconds (s^{-1}). The standard error for the oxidation rate was determined by a least-square fit of the data at each measured condition.

The normalized weight loss as a function of exposure time showed the impact of temperature and P_{H2O} on oxidation at test conditions relevant to accident conditions. Figure 6 shows normalized weight loss as a function of time for 1,200°C over the range of analyzed $P_{H2O,}$ which illustrates the impact of the oxidant concentration. Figure 7 shows the oxidation behavior at $P_{H2O} = 10$ kPa for test temperatures from 1,200–1,500°C, which illustrates the impact of temperature at a constant P_{H2O}. A linear fit was applied to the data to determine the oxidation rate (s^{-1}), and Table 18 shows the results of the rate analysis and associated uncertainty of the fit. The analysis indicated that the oxidation rate increased with increasing

P_{H2O} up to 30 kPa for test temperatures from 1,200–1,400°C. Testing at 1,200°C also included a test at P_{H2O} = 48 kPa that showed a similar rate to that at P_{H2O} = 30 kPa, suggesting a saturation effect at 1200°C below P_{H2O} = 48 kPa. The behavior at 1300°C and 1400°C both showed increasing rates as a function of P_{H2O}, however, no P_{H2O} = 48 kPa conditions were explored at these temperatures.

The constant pressure analysis shown in Figure 7 highlights the overall impact of temperature. This analysis clearly indicates that oxidation increases with increasing temperature, as expected in a kinetic process. Multiple tests were run for select conditions at P_{H2O} = 20 kPa to determine the repeatability of the analyses. Variation in the measured normalized weight loss was observed. The variability is not expected to be due to density differences. At 1,200°C, P_{H2O} = 20 kPa, 2 hours exposures, the densities of the three samples ranged from 1.783–1.792 g/cm^3, which represents only a 0.33–0.84% difference in density. However, this does not reflect the overall increase in weight loss observed across the three samples, which showed an ~49% difference in magnitude between the lowest recorded weight loss and the maximum weight loss for this analyzed condition. The variation is expected to be associated with microstructural feature variation such as exposed pore structure and fissures, which were expected and observed in the matrix-only blank samples produced with the AGR-5/6/7 matrix formulation (Hunn et al. 2011).

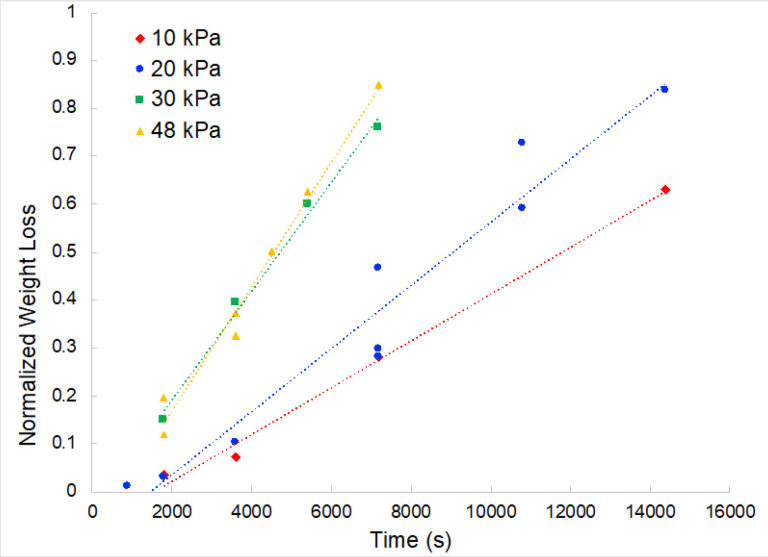

Figure 6. Normalized weight loss as a function of time for tested P_{H2O} at 1,200°C.

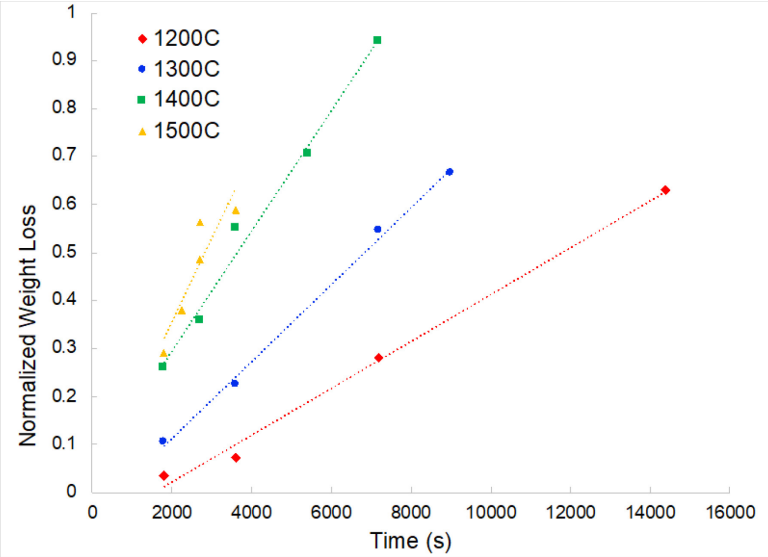

Figure 7. Normalized weight loss as a function of time for tested temperatures at P_{H2O} = 10 kPa.

The measured rates presented in Table 18 were fit to an Arrhenius relationship, defining an effective rate equation for each analyzed P_{H2O}. Table 19 lists the activation energy (E) and pre-exponential term (A) associated with the Arrhenius relationship. The Arrhenius relationship is empirically derived and appropriate only over the range of conditions (including oxidant flow rate) analyzed.

Table 18. Rate analysis for high-temperature oxidation testing

Temperature (°C)	P_{H2O} (kPa)	Rate (s^{-1}) [a]	R^2 [b]
1200	10	$4.89\pm0.26\times10^{-5}$	0.99
1200	20	$6.59\pm0.60\times10^{-5}$	0.95
1200	30	$1.13\pm0.07\times10^{-4}$	0.99
1200	48	$1.30\pm0.08\times10^{-4}$	0.98
1300	10	$8.03\pm0.32\times10^{-5}$	1.00
1300	20	$1.37\pm0.09\times10^{-4}$	0.97
1300	30	$1.90\pm0.21\times10^{-4}$	0.97
1400	10	$1.25\pm0.09\times10^{-4}$	0.99
1400	20	$1.86\pm0.26\times10^{-4}$	0.91
1400	30	$3.71\pm0.36\times10^{-4}$	0.96
1500	10	$1.71\pm0.45\times10^{-4}$	0.83

[a] Error is reported as standard error from linear regression analysis.
[b] R^2 values are rounded to two significant figures.

Table 19. Effective oxidation kinetics for matrix-only samples in high-temperature steam

P_{H2O} (kPa)	A (s^{-1})	E (kJ/mol)
10	0.09	91.6
20	0.43	107.1
30	2.18	121.3

Samples were axially cross sectioned and optically imaged to show the nature of the oxidation behavior. Figure 8 shows a series of optical micrographs from an as-fabricated sample and from samples

exposed to 1,200°C for 1 hour at different P_{H2O} (20–48 kPa). Fissures running perpendicular to the pressing direction were identified in the as-fabricated samples (Figure 8a). The presence of fissures was not unexpected based on previous observations for this matrix recipe (Hunn et al. 2011). A uniform oxidation layer was apparent around the outer surface of the oxidized samples (Figure 8b–d) with an apparently unaffected central region. Localized oxidation penetrating the bulk was also observed along the inner surface of fissures intersecting the surface. This oxidized region appeared to have a lower overall density relative to the bulk. The low-density oxidized regions are indicated in the figure by a darker color relative to the bulk and an increased porosity. Some pores and fissures are filled with epoxy (gray), while those that were not infiltrated with epoxy appear black. The fissures serve as pathways for oxidation to penetrate the interior of the sample. Clear evidence of this is shown in the close-up micrograph in Figure 9a, in which oxidation had preferentially occurred along the exposed surface of a fissure that intersected the sample surface. The samples exposed to higher P_{H2O} showed significant oxidation along the fissures, leading to nonuniform oxidation of the sample. A close-up micrograph of an oxidation region is shown in Figure 9b. In this figure, the low-density oxidized material has flake-like grains surrounded by epoxy, with an apparent gradient from loose graphitic flake to denser matrix material moving from the exposed surface toward the bulk, where oxidation was less significant.

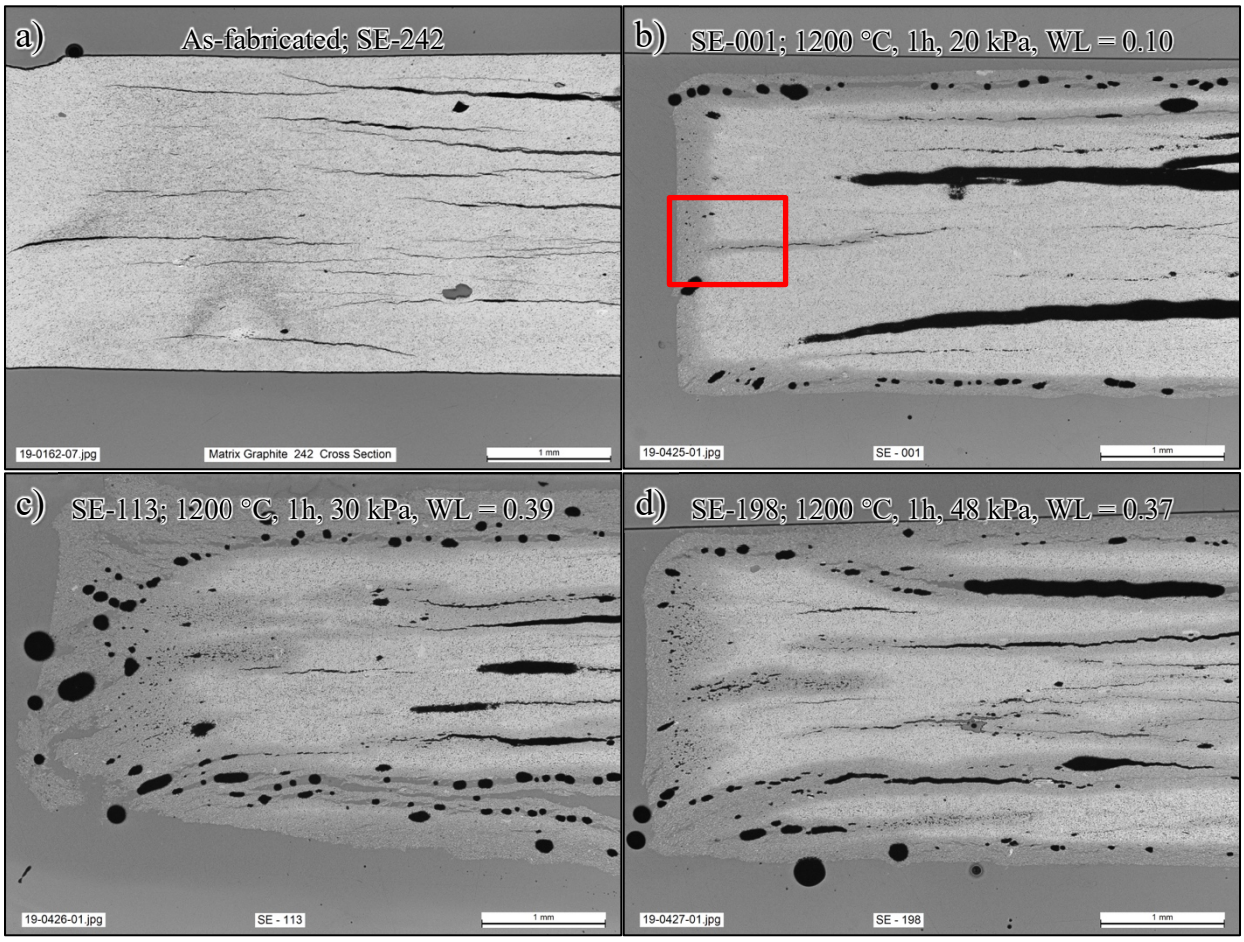

Figure 8. Overview micrographs of the cross-section of an as-fabricated and select samples oxidized at 1,200°C for 1 hour with varying P_{H2O} showing the impact of macroscopic fissures on oxidation behavior in the high-temperature oxidation testing (the red box in (b) identifies the approximate area of interest presented in Figure 9a; black regions are pores not filled by epoxy; and *WL* is the normalized weight loss).

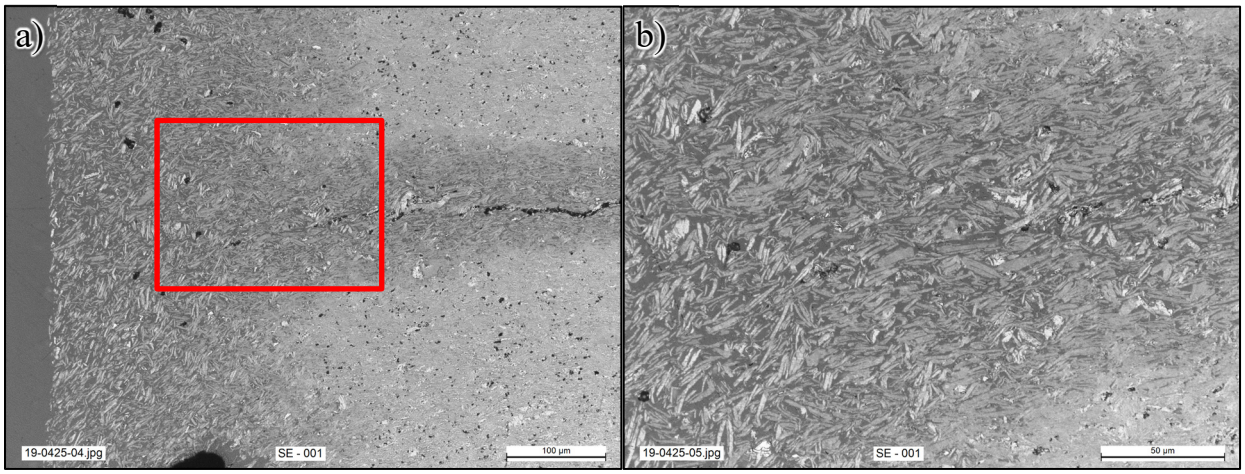

Figure 9. Close-up micrographs from SE-001 (1,200°C, 1 hour, P_{H2O} = 20 kPa) highlighting penetration along the exposed fissures and low-density oxidized region with apparent residual graphite flake. The red box in (a) shows the area of interest imaged in (b) at higher magnification.

The preferential oxidation observed at the surface confirms that the oxidation reaction is beyond the purely kinetic regime as there is clearly a partially oxidized region penetrating from the surface. However, the matrix-only samples are not a heterogenous material, as they consist of a partially graphitized resin binder, natural graphite flake, and synthetic graphite flake. Each of these components is expected to have a different oxidation response. Because of the composite nature of the matrix-only samples, it is possible that the reaction is in the diffusion-controlled regime for the partially graphitized resin binder and in the transition regime for the graphite flake components, as they appear to preferentially remain in the low-density, oxidized regions.

The optical micrographs in Figure 8 and Figure 9 confirm the influence of exposed surface area on the oxidation behavior. The distribution of fissures in the samples likely explains the observed sample variance in the high-temperature empirical oxidation tests. The presence of exposed fissures increased the effective surface area. In the kinetic regime, this would not impact the results, as the oxidation occurs uniformly. However, in the transition and diffusion-controlled regimes for graphite oxidation, the oxidation reaction is surface dependent, so the increased effective surface area will lead to an increase in the overall oxidation rate.

The high-temperature empirical oxidation rate data for 1,200–1,400°C obtained from tests in the HTM are compared with the oxidation kinetics data from the lower-temperature TAG analyses in Figure 10. Figure 10 shows the LH and BLH model fits to the data acquired from the TAG analysis, which produced the kinetic parameters listed in Table 17. The data points for P_{H2O} below 1,000 Pa are from the TAG analysis to which the LH and BLH models were fit. The data points for $P_{H2O} \geq$ 10,000 Pa are from the HTM tests. Figure 11 shows the observed vs. predicted rates for measured oxidation data for the LH and BLH models, with high-temperature empirical oxidation results included. The correlation coefficient (R^2) for each fit with the high temperature data included is 0.98 for the LH model and 0.97 for the BLH model. The BLH model shows good agreement with the 1,200°C data based on the comparison of the predicted rate vs. the measured oxidation rate. This corroborates the assessment that the BLH model better captures the oxidation behavior at higher temperatures and P_{H2O} (Contescu, Lee, and Mee 2018). The appropriateness of the BLH model at 1,200°C should be questioned, as the destructive analysis indicates that the samples are beyond the kinetic regime. This is supported for the higher temperature conditions in which both models overpredict the oxidation rates at 1,300°C and 1,400°C. This is expected to be a result of the oxidation no longer being in the kinetic regime at the elevated temperatures. The optical micrographs indicate that oxidation was in the transition regime where both

chemical kinetic and mass transfer phenomena were significant. An accurate model for that regime would have to include both of these effects.

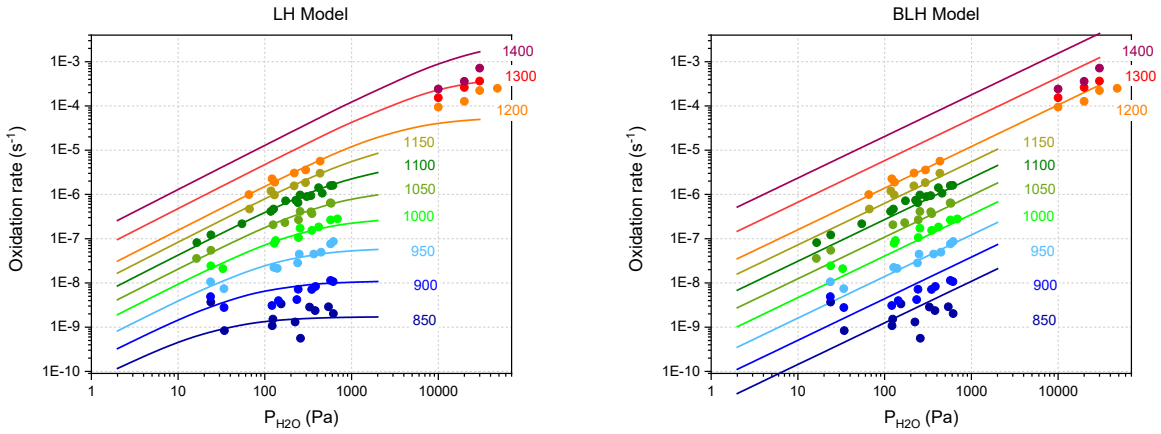

Figure 10. Experimental oxidations rates at $P_{H2} = 0$ with isothermal trend lines reflecting kinetic parameters determined from best fit for LH and BLH models with high temperature empirical oxidation results included.

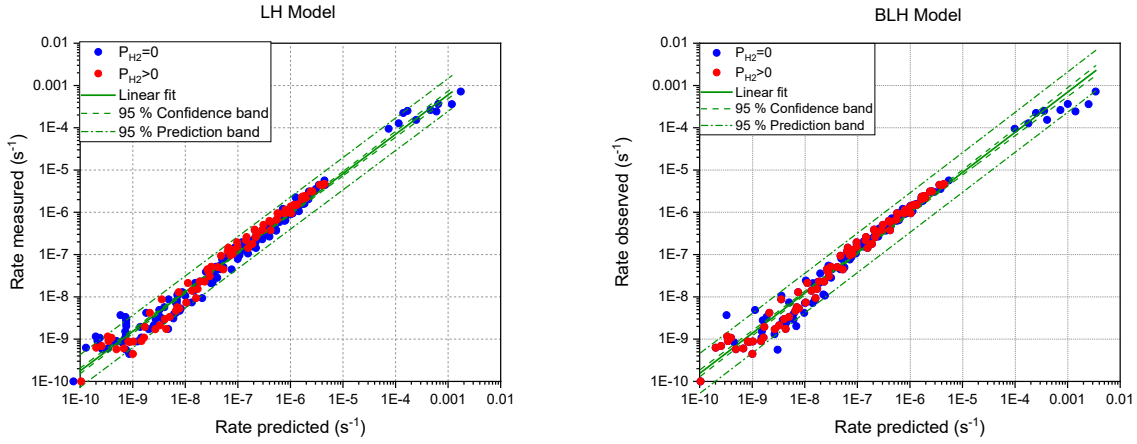

Figure 11. Observed versus predicted rate for measured oxidation data for the LH and BLH models with high temperature empirical oxidation results included.

2.1.2.1.4 Conclusions from Oxidation Testing of Matrix Material

This study established separate effects testing of the oxidation performance of HTGR matrix material in varied moisture environments. Investigation of the oxidation behavior was conducted over a wide range of oxidation conditions that spanned the kinetic regime and beyond. The range in conditions allowed for analysis of the chemical oxidation kinetics and the conditions relevant to extreme accident scenarios. The oxidation rate data in the oxidation kinetics evaluation were fit to two established models—LH and BLH—to determine the kinetic parameters (Table 17). Both models fit the data reasonably well, with the LH model better representing the data at lower temperatures and pressures (P_{H2O}), and the BLH model better representing the data at higher temperatures and pressures (P_{H2O}). This observation is consistent with prior analysis conducted for nuclear-grade graphite. Ultimately, the kinetic parameters that were obtained can be leveraged in fuel performance models to determine the response of matrix material in various scenarios involving moisture ingress. The empirical oxidation testing at high

temperatures (1200°C ≤ T ≤ 1500°C) and high pressures (P_{H2O} ≥ 10 kPa) showed the expected trends, with increasing oxidation rate as a function of temperature. At a constant temperature, the testing showed oxidation rates increased with increasing P_{H2O}, with apparent saturation at 1200°C below 48 kPa. An Arrhenius relationship was fit to the varying oxidation rates at a given P_{H2O}. Comparison of the empirical high temperature, high-P_{H2O} oxidation rates with the LH and BLH models showed that the models overpredicted the oxidation rate. This is justified, since a departure from the kinetic regimes into a surface-sensitive, diffusion dependent regime is expected and was confirmed based on the observed deviation from the LH and BLH fits and by the surface dependence of the oxidation reaction shown in the optical microscopy of cross sectioned samples. This destructive analysis also highlighted the composite nature of the matrix-only samples, in which apparent selective oxidation of the carbonized resin binder was occurring, as residual graphite flake material appeared to be remaining in the oxidized surface regions. Furthermore, the fissures in the samples acted as pathways for transport of oxidants from the sample surface to the interior. Differences in the number and structure of fissures from sample-to-sample also led to apparent variation in sample oxidation rate at higher temperatures and partial pressures that were beyond the kinetic regime. Sample-to-sample variation was not observed in the kinetic regime tests because kinetic oxidation occurred more uniformly throughout the sample and was not limited by oxidant mass transport effects that became more significant at higher temperatures.

Future work should target oxidation testing of matrix-only samples without fissures to isolate the high temperature matrix oxidation behavior, given the variation of oxidation response in matrix material with fissures during testing beyond the kinetic regime. This testing would be more representative of a separate effects test. Matrix material from the AGR-1 and AGR-2 experiments may satisfy this case. A systematic pursuit of precursor materials (natural graphite flake, synthetic graphite flake, and binder resin), matrix formulations, and processing routes may also be warranted. This would allow the exploration of fully dense material with minimal defects such as fissures or pores as well as materials with different microstructures. The motivation is to understand how the defect structure and matrix microstructure impacts the response to interactions with oxidants. Other areas of relevant pursuit may involve oxidation tests of surrogate fuel compacts containing non-fueled particles to better simulate the microstructure in graphitic matrix material of actual fuel elements. The presence of fuel particles during fuel form pressing impacts the local matrix density and orientation of graphite flake.

2.1.2.1.5 References

Contescu, C. I., et al. 2008. “Practical Aspects for Characterizing Air Oxidation of Graphite.” *Journal of Nuclear Materials* 381: 15–24.

Contescu, C. I., T. D. Burchell, and R. W. Mee. 2013. *Accelerated Oxidation Studies of PCEA Nuclear Graphite by Low Concentrations of Water and Hydrogen in Helium.* ORNL/TM-2013/524. Oak Ridge, TN: Oak Ridge National Laboratory.

Contescu, C. I., R. W. Mee, et al. 2014. “Oxidation of PCEA Nuclear Graphite by Low Water Concentrations in Helium.” *Journal of Nuclear Materials* 453: 225–232.

Contescu, C. I., T. D. Burchell, and R. W. Mee. 2015. *Kinetics of Chronic Oxidation of NBG-17 Nuclear Graphite by Water Vapor.* ORNL/TM-2015/142. Oak Ridge, TN: Oak Ridge National Laboratory.

Contescu, C. I., Y. J. Lee, and R. W. Mee. 2018. *Oxidation Kinetics by Water Vapor of Nuclear Grade Graphite Grade 2114.* ORNL/TM-2018/1057. Oak Ridge, TN: Oak Ridge National Laboratory.

Contescu, C. I., and R. Mee. 2018. *Status of Chronic Oxidation Studies of Graphite.* ORNL/TM-2016/195. Oak Ridge, TN: Oak Ridge National Laboratory.

Contescu, C. I., R. W. Mee, Y. J. Lee, J. D. Arregui-Mena, N. C. Gallego, T. D. Burchell, J. J. Kane, and W. E. Windes. 2018. “Beyond the Classical Kinetic Model for Chronic Graphite Oxidation by Moisture in High Temperature Gas-Cooled Reactors.” *Carbon* 127: 158–169.

Gerczak, T. J., C. I. Contescu, Y. J. Lee, R. W. Mee, A. T. Schumacher, J. D. Stempien, and M. P. Trammell. 2019. *Oxidation of matrix material in helium with varied moisture content.* ORNL/TM-2019/1341. Oak Ridge, TN: Oak Ridge National Laboratory.

Giberson, R. C., and J. P. Walker. 1966. "Reaction of Nuclear Graphite with Water Vapor. Part I. Effect of Hydrogen and Water Vapor Partial Pressures." *Carbon* 3: 521–525.

Hunn, J. D., M. P. Trammell, and F. C. Montgomery. 2011. *Data Compilation for AGR-3/4 Matrix Ring Blank Lot ARB-B1.* ORNL/TM-2011/272. Oak Ridge, TN: Oak Ridge National Laboratory.

Hurt, T. H., and J. M. Calo. 2001. "Semi-Global Intrinsic Kinetics for Char Combustion Modeling," *Combustion and Flame* 125: 138–1149.

Overholser, L. G., and J. P. Blakely. 1965. "Oxidation of Graphite by Low Concentrations of Water Vapor and Carbon Dioxide in Helium." *Carbon* 2: 385–394.

Walker, Jr., P. L., F. Rusinko, Jr., and L. G. Austin. 1959. "Gas Reactions of Carbon." *Adv. Catalysis* 11: 133–221.

Velasquez, C., G. Hightower, and R. Burnette. 1978. *The Oxidation of H-451 Graphite by Steam.* GA-A14951. San Diego, CA: General Atomics.

2.1.2.2 Received all Radiochemical Data from Pacific Northwest National Laboratory (PNNL) Following INL's Physical Sampling of AGR-3/4 Capsule 10 Inner and Outer Rings

2.1.2.2.1 AGR-3/4 Experiment Background

As shown in Figure 12, each AGR-3/4 irradiation capsule had four compacts stacked in the center of a hollow cylinder (inner ring) of nuclear graphite (PCEA or IG-110) or graphitic matrix material (A3-27). Each compact contained 20 designed-to-fail (DTF) particles and 1872 TRISO-coated driver particles. The DTF particles were coated only with a 20 μm thick pyrocarbon layer with a high anisotropy that made the pyrocarbon likely to fail during irradiation. An intact DTF particle would behave like a TRISO particle with a failed SiC layer, releasing metallic fission products, but retaining fission gases. A failed DTF particle would behave like a fuel particle with a failed TRISO coating. The DTF particles acted as a source of fission products. The inner ring was nested within an outer ring of nuclear graphite. Fission products escaping the compacts migrated radially outward to the inner ring and then to the outer ring. The goal of the experiment was to enable measurements of fission-product transport parameters (i.e., diffusion coefficients) in graphite and graphitic materials.

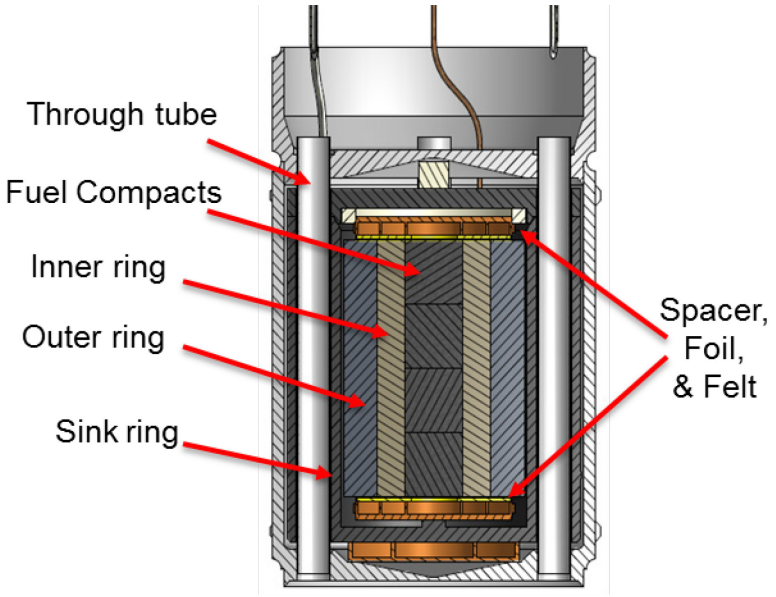

Figure 12. Axial cutaway of a “standard” AGR-3/4 irradiation capsule.

2.1.2.2.2 AGR-3/4 Ring Sampling Process

The inner and outer rings from AGR-3/4 Capsules 3, 5, 7, 8, 10, and 12 have been physically sampled using specialized equipment in the HFEF main cell at INL. Figure 13 shows drawings of the equipment and example images of rings at various stages of sampling. Physical sampling of AGR-3/4 rings involved the use of an end-mill to radially remove material from the rings, a cyclone separator to collect that material, and then a series of methods to analyze the fission-product content in the collected material. The samples generated from sampling were sent to PNNL for measurement of gamma emitting fission products, Sr-90, and analysis by inductively couple -plasma mass spectrometry. Upon completion of the measurements, PNNL transmitted data to INL for interpretation and construction of fission-product profiles.

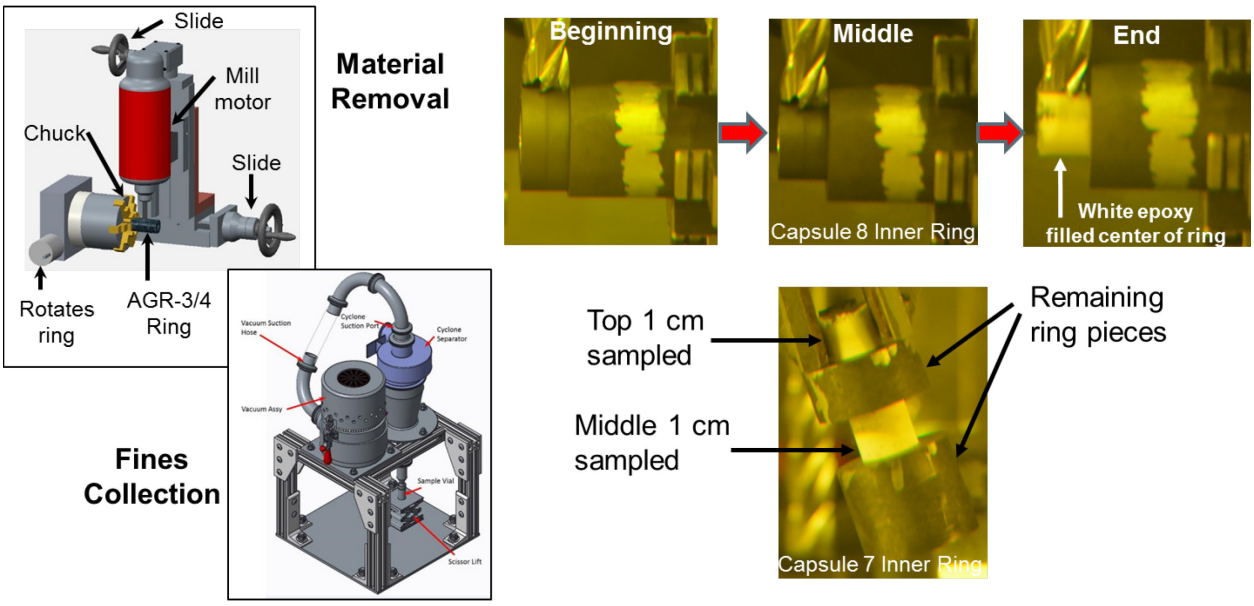

Figure 13. End-mill for ring milling/material removal. Cyclone separator for fines/material collection. Images of the Capsule 8 inner ring at three times during the sampling procedure. Image of the Capsule 7 inner ring after sampling at the axial top and axial center had been completed.

2.1.2.2.3 Completed Capsule 10 Radial Fission-Product Profiles

Completed fission-product radial profiles were shown in the ART FY 2018 Q4 Report (INL/EXT-18-44496) for the inner and outer rings of Capsules 3, 5, 7, and 8. Figure 14 and Figure 15 show the complete radial fission-product profiles for the center and bottom of the Capsule 10 inner and outer rings, respectively. It is noteworthy that the during the bottom cut of OR-10, the ring came loose in the milling machine. Therefore, only cuts 1 and 2, and 8 through 12, were deemed to be completely reliable. Even with the uncertainty on cuts 3 through 7, those data points are similar to the unaffected cuts. The shapes of the profiles and the behavior at the inner and outer surface of the rings are similar to earlier observations for the Capsule 3, 5, 7, and 8 rings.

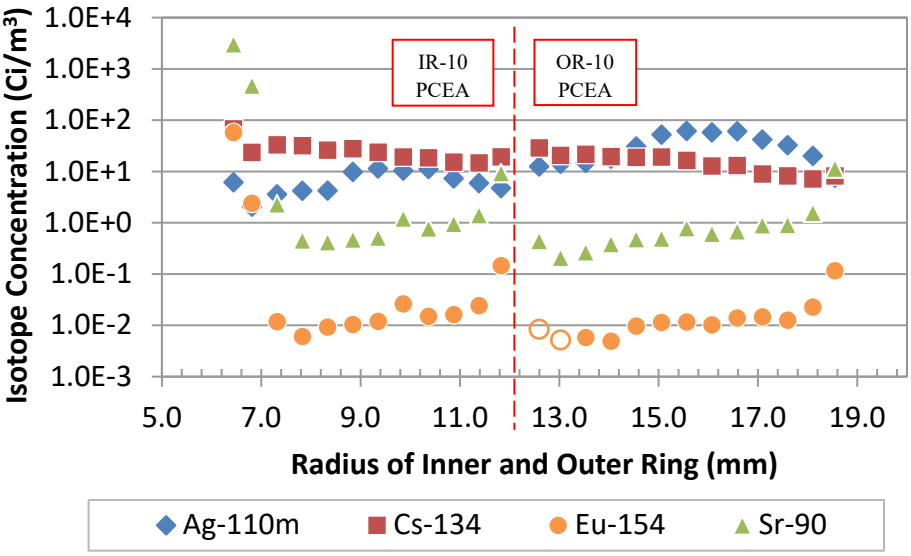

Figure 14. Radial fission-product concentration profiles for select isotopes from the axial center of AGR-3/4 Capsule 10 inner and outer rings. Open symbols indicate points that were estimated from minimum detectable activities.

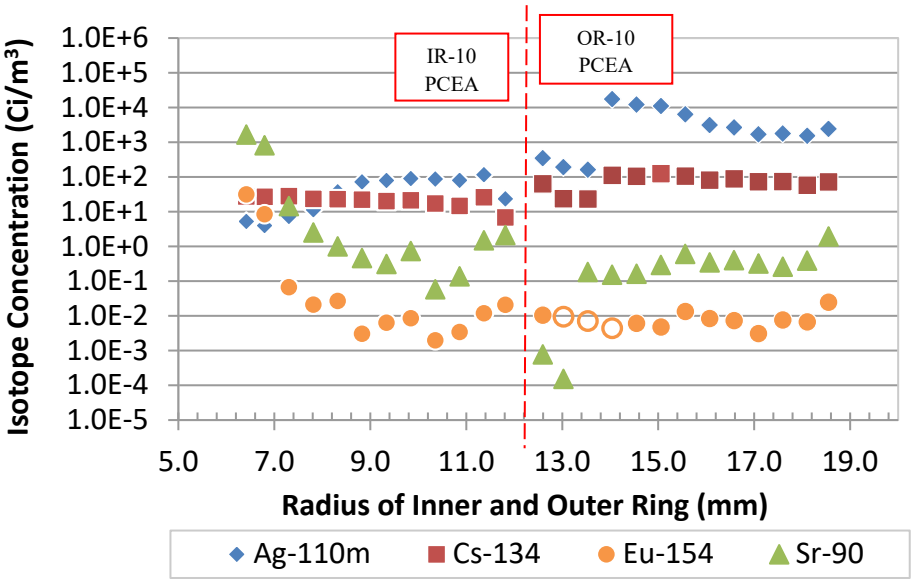

Figure 15. Radial fission-product concentration profiles for select isotopes from the axial bottom of AGR-3/4 Capsule 10 inner and outer rings. Open symbols indicate points that were estimated from minimum detectable activities.

2.1.2.3 Update on AGR-3/4 Fuel Compact Radial Deconsolidation

A key data need in the AGR-3/4 fission-product transport analysis is the inventory of fission products residing outside of the compact matrix. Standard DLBL analysis would be ineffective for determining this, since it would result in dissolution of the exposed DTF kernels during the process. The radial deconsolidation-LBL (R-DLBL) process was developed to address this need. In this method, materials (matrix debris and particles) are removed around the circumference of the compact in several steps of known thickness. The deconsolidation solution and particles from each step are analyzed to determine a radial profile of fission-product concentrations in the compact outside of the particle SiC layer. The final

step of the R-DLBL is the axial deconsolidation of the core of the compact that contains the DTF particles. Seven compacts have undergone R-DLBL, and additional compacts in the as-irradiated condition and after high temperature post-irradiation heating tests in the FACS furnace will undergo R-DLBL.

2.1.2.3.1 Procedure

Figure 16 provides a graphical representation of the radial deconsolidation process. At far left, the compact image is an x-ray radiograph. The red dots highlight the location of DTF particles. The white dots are fully TRISO-coated driver particles. The compact is mounted to a stainless-steel rod using epoxy. The compact is then partially immersed in a nitric acid solution (in which a platinum wire serves as the cathode), held in contact with a platinum screen (serving as the anode), and rotated at 10 rpm. After approximately 15 minutes of compact rotation with a voltage applied across the cathode and anode, the compact is raised up out of the acid solution and a video is acquired. The video of the rotating compact is used to measure the diameter of the compact. The image with the green background is a frame from the video analysis where the compact is shaded blue and three red lines are overlaid to show the center and upper and lower edges of the rod. Two or three more 15-minute deconsolidation segments are performed. What remains at the end of the radial deconsolidation of the compact is a thin core that contains the driver particles. This core is deconsolidated in a single step. A collection of loose particles and a deconsolidation solution are collected after each of the three to four radial steps and after the final axial deconsolidation of the core.

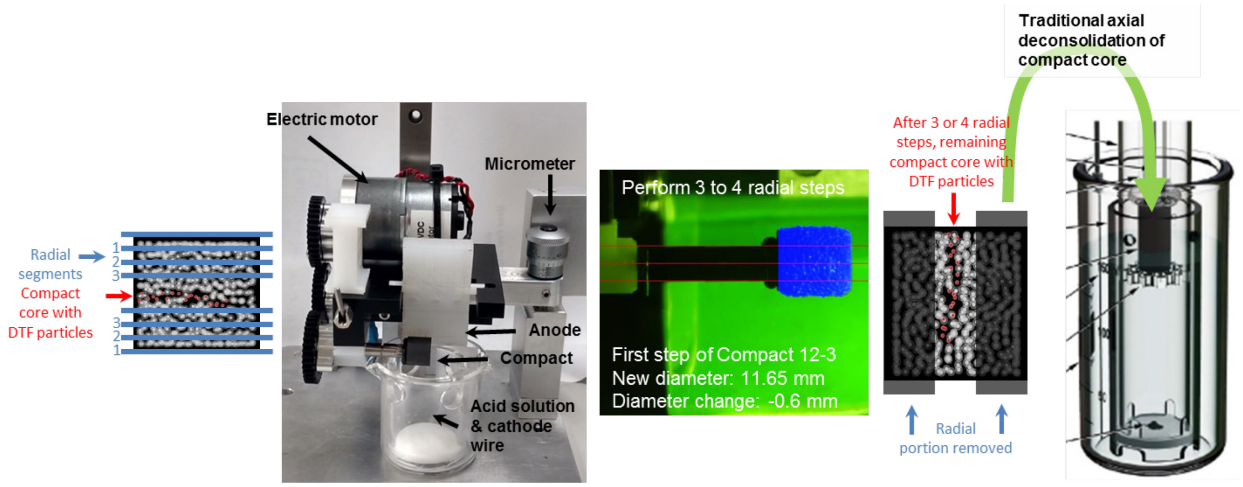

Figure 16. Flow diagram of the AGR-3/4 compact radial deconsolidation process.

2.1.2.3.2 Selected Profiles from Compacts 5-3 and 5-4

It takes roughly 8 to 12 months to complete the radiochemical analysis from one R-DLBL. The profiles from the R-DLBL of Compacts 5-3 and 5-4 (deconsolidated at the end of FY-18) are shown in Figure 17 and Figure 18, respectively. Profiles for Compacts 3-3 and 12-1 were shown previously in the ART FY 2019 Q4 report. Generally, the fission-product inventory decreases from the central core to the innermost one or two radial segments. However, there is an apparent increase in the concentration of all three selected fission products at the surface of Compact 5-3. Compact 5-4 shows an increase of the Cs-134 concentration at its surface. The reason for this is not clear. Compacts 8-2 and 3-2 will undergo R-DLBL in FY-20 at INL. Two additional compacts will undergo R-DLBL at ORNL in FY-20. These data are being used for comparison to existing model comparisons and as input to models for calculating diffusion coefficients for fission products in graphite and graphitic matrix material.

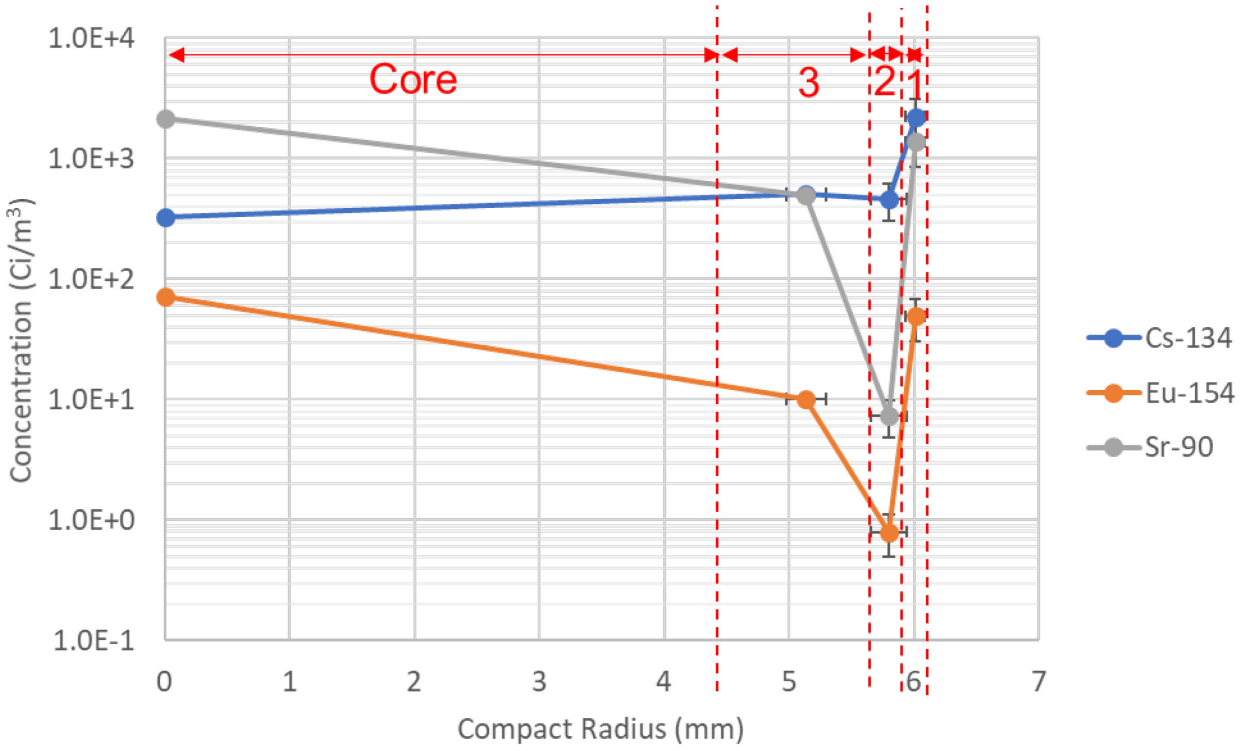

Figure 17. Profile of select fission products from R-DLBL of as-irradiated AGR-3/4 Compact 5-3.

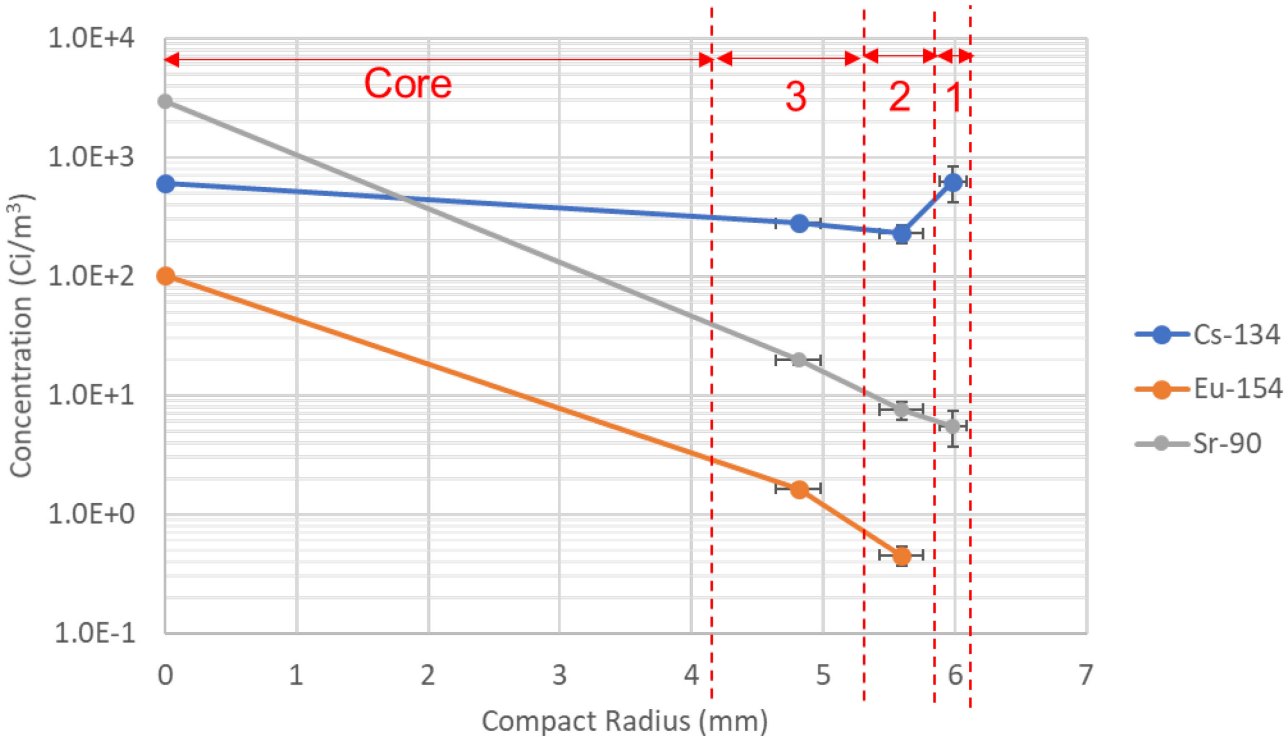

Figure 18. Profile of select fission products from R-DLBL of as-irradiated AGR-3/4 Compact 5-4.

2.1.2.4 Advanced Microscopic Analysis of Particle AGR2-222-RS019

TEM data such as scanning (S)TEM imaging, chemical analysis by EDS, and precision electron diffraction (PED) have been collected on Location A and B (see Figure 19) of neutron irradiated AGR2-222-RS019 particle. The basis for selection of these location is the gap in the buffer layer (as seen in Location B) and intact buffer layer (as seen in Location A). The lamella from Location A are numbered lamella 1 through 3 from the inside to the outside of the SiC layer. Lamella from Location B are numbered Lamella 5 through 7 from the inside of the SiC layer to the outside of the SiC layer. Figure 20 shows Lamella 5 as a representative Lamella for this quarterly report. Lamella 5 is at an interface between the IPyC layer and the SiC layer. The red boxes at left in Figure 20 highlight the areas of Lamella 5 that were analyzed by EDS and PED. The other lamellae were also analyzed in three areas. The grain boundary precipitates and large-scale precipitates, mostly at triple junctions, were analyzed by spot-EDS. While the grain boundary usually contains Pd as the main fission-product, the large precipitates are often found to be composed of Pd, U, and Pu.

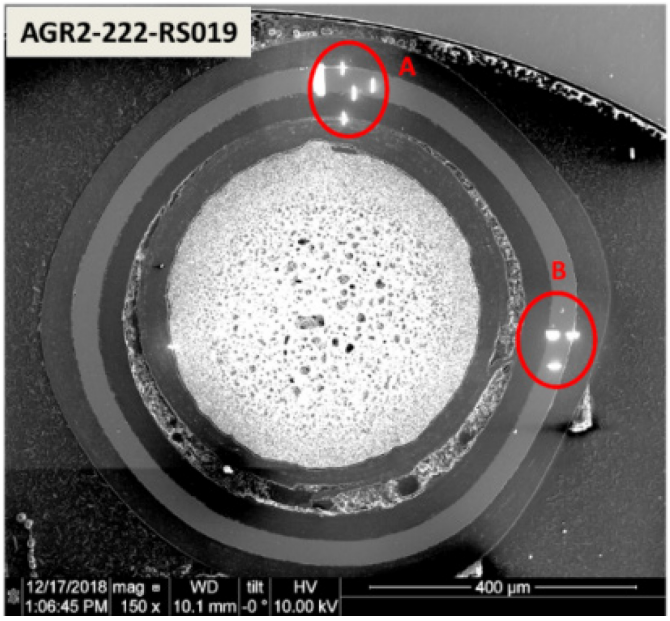

Figure 19. The scanning electron microscopy (SEM) images shows the TEM plan from location A and B for detailed characterization of SiC layer of neutron irradiated TRISO particles.

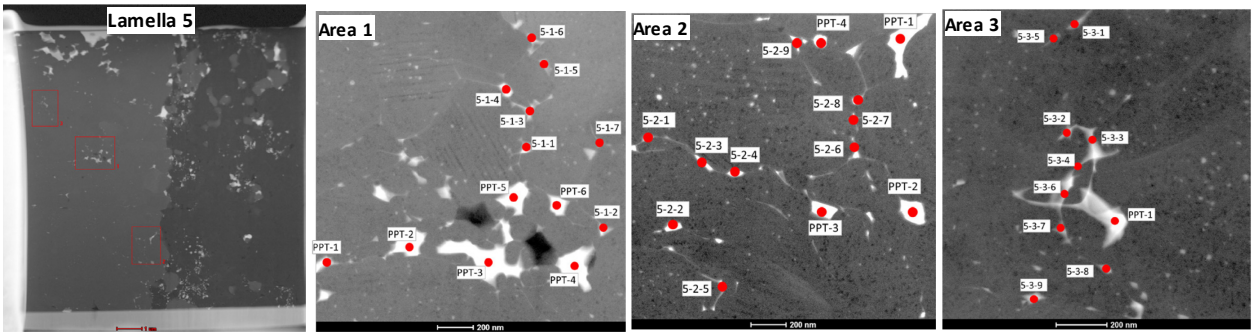

Figure 20. The STEM image of Lamella 5 shows all the three areas chosen for coupled EDS and PED analysis. This compilation shows all the areas of Lamella 5 chosen for analysis. The areas were analyzed with spot EDS for chemistry of grain boundary precipitate and large-scale precipitates.

To understand the nature of grain boundary precipitate chemistry, knowledge of the nature of the grain boundaries is needed. Accordingly, PED has been performed for all areas of each lamella for a comprehensive understanding of grain boundary character and grain boundary precipitate chemistry. Figure 21 shows the coupled EDS and PED analysis on Area-1 of Lamella 5.

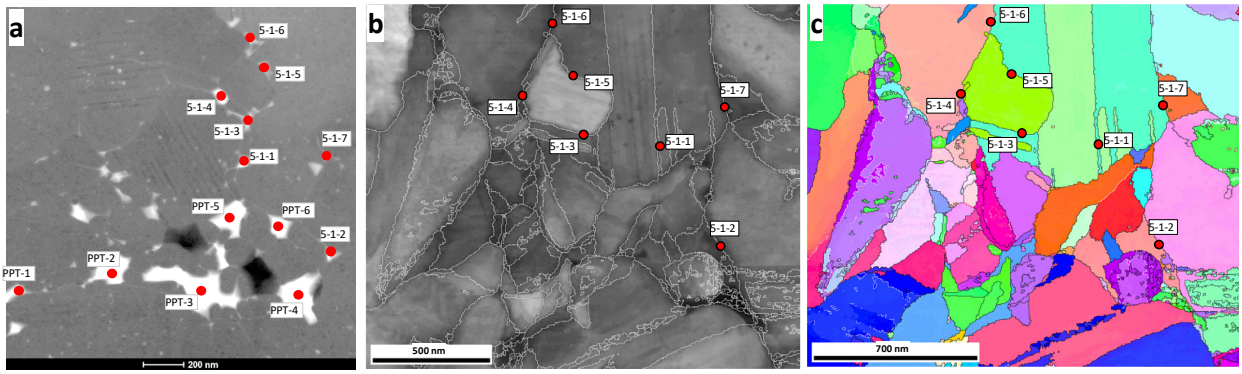

Figure 21. This compilation shows the coupled EDS and PED analysis on Area-1 of Lamella 5. (a) a STEM image, (b) an image quality micrograph and (c) an orientation map of grains corresponding to the same area as represented in in STEM image in (a).

2.2 High-Temperature Materials Development

Highlights of high-temperature materials activities during October, November, and December 2019 are as follows:

The work this quarter can be separated into three focuses: 1) addressing issues flagged by an NRC-sponsored assessment of a previous version of Section III, Division 5 of the ASME BPVC, 2) acquiring data for code needs, and 3) probing the incorporation of advanced manufactured materials and components into Section III, Division 5 of the ASME BPVC. INL staff attended the October ASME Boiler Code Week. They participated in numerous committee meetings including the working groups on Creep-Fatigue and Negligible Creep and Allowable Stress Criteria. INL staff also assisted in developing a charter for a new task group on Section III Division 5 advanced manufactured materials and components. The goal of this task group is to develop Code Actions for Section III, Division 5 code qualification of advanced manufactured materials and components. This task group will commence at the February 2020 Boiler Code week. INL staff will participate in this task group including acting as chair and secretary. INL's participation at the Boiler Code Week enables better tailoring of work to address the focuses stated above.

An inadequate understanding of the impact of multiaxial stress, structural discontinuities, and notches was identified by the NRC-sponsored assessment mentioned above as needing addressed (Huddleston, 1993). Two specimen geometries, U-notch and V-notch, were utilized to resolve this. The U-notch specimen, also known as a Bridgeman-notch, were used to generate a multiaxial-stress state. Two different notch geometries were employed to analyze two different multiaxial-stress states. The V-notch specimen is comprised of a V-notch and straight gauge with the same diameter. It enables the notch behavior to be qualitatively evaluated for a given temperature and stress. The notch can be categorized as notch strengthening or weakening depending on if the rupture occurs in the straight gauge or V-notch, respectively. This investigation validated using short-term design rules established from uniaxial data. This conclusion is best highlighted by the Larson-Miller Curve shown in Figure 22 below. The time to rupture Larson-Miller curve from the Section III, Division 5 code case is shown (Wright, 2015). Overlaid is creep-rupture data from the following sources: 1) base-metal uniaxial data of known chemistry compiled from multiple heats and product form (Wright, 2015), 2) uniaxial, V-notch, and U-notch base-metal data from Heat 314626 (Wright, 2015), and 3) uniaxial, V-notch, and U-notch weld-metal data

from Heat XX3703UK (Natesan, 2012)(Wright, 2014). From Figure 22 it is apparent that both the base- and weld-metal V-notch and U-notch data fell within the scatter of compiled uniaxial base-metal data of known chemistry from various products and heats. Furthermore, the V-notch and U-notch data for both the base- and weld-metal fell on or to the right of the uniaxial data from the equivalent heat. This indicates that the V-notch and U-notch specimens had equivalent or improved creep-rupture lives compared to uniaxial data.

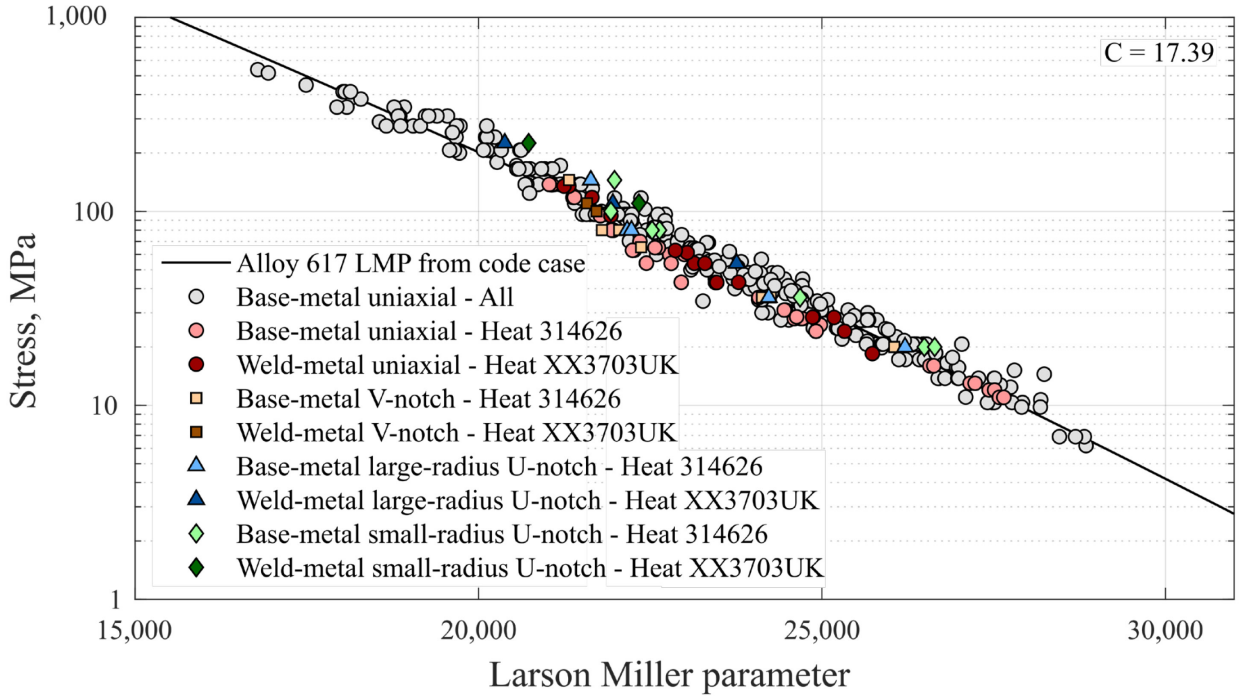

Figure 22 The time to rupture Larson-Miller Curve from the Alloy 617 ASME BPVC Section III, Division 5 code case with the following creep-rupture data overlaid: 1) base-metal uniaxial data of known chemistry compiled from multiple heats and product form, 2) uniaxial, V-notch, and U-notch base-metal data from Heat 314626, and 3) uniaxial, V-notch, and U-notch weld-metal data from Heat XX3703UK.

There is an ongoing endeavor to assess various damage models. This entails comparing experimental There is an ongoing endeavor to assess various damage models. This entails comparing experimental observations of creep damage to finite element model predictions. Creep damage in base-metal U-notch specimens have been quantified. The non-ruptured notch in U-notch specimens consisting of two U-notches with the same geometry were analyzed. This enabled the damage just prior to failure to be analyzed. The creep damage void fraction as a function of distance from the center of the notch was calculated. Both large- and small-radius creep-rupture specimens as a function of distance were quantified for both the longitudinal and radial direction. The results are shown in Figure 23 below. From Figure 23 it is apparent that damage in the longitudinal direction varies between the small-and large radius U-notch. This indicates creep damage is impacted by the multiaxial stress state. So far, this work has been limited to assessing the damage models with respect to multiaxial stress caused by a U-notch. It is desired to expand this assessment to a V-notch structural discontinuity. Therefore, work is in progress to perform creep-rupture tests with a specimen comprised of two V-notches. An engineering drawing for the

machining of this specimen has been drafted and approved. These double V-notch specimens are currently being machined and will be ready for testing next quarter.

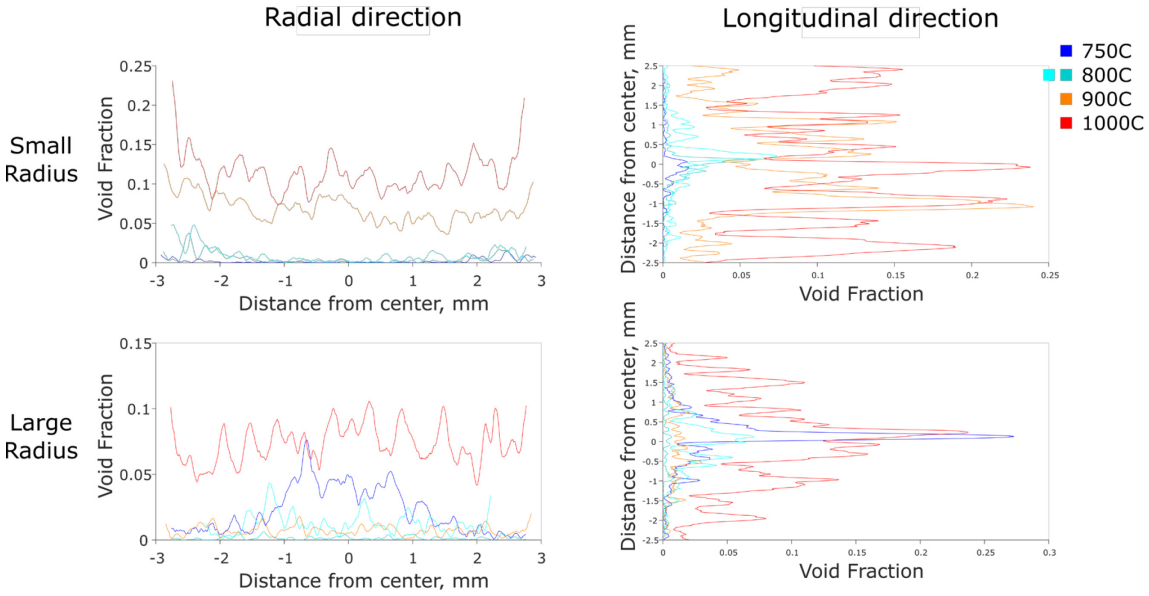

Figure 23: The creep damage void fraction as a function of distance from the center of the non-ruptured U-notch. Both large- and small-radius specimens are analyzed in the radial and longitudinal direction.

Notch-rupture behavior is sensitive to variations in stress and temperature. Consequently, short-term (~1,000 hours) creep-rupture testing may not accurately represent notch behavior for long-term (~100,000 hours) service lives. Therefore, intermediate and long-term creep-rupture testing is necessary. It is not practical, however, to wait 100,000 hours to learn the outcome of a test. This necessitated developing a methodology to determine the rupture location prior to failure. X-ray CT was chosen to serve this purpose as it can non-destructively characterize creep damage. This requires knowledge of the relationship between creep damage and rupture life. Therefore, shorter baseline testing to establish this relationship were necessary. Two baseline tests with estimated rupture lives of 4,800 and 8,000 hours are ongoing. The specimen with a 4,800 hour rupture life has been characterized twice with X-ray CT at 2,005 and 2,500 hours. Representative images from these scans are shown in Figure 24 below. Cavities were observed throughout the straight gauge after 2,005 and 2,500 hours of testing. Longer test times resulted in an increase in the size and number of cavities. The V-notch was free of cavitation for both scan times.

There are seven intermediate and two long-term ongoing creep-rupture tests. These specimens have a targeted rupture life of 12,000 to 16,000 and 100,000 hours, respectively.

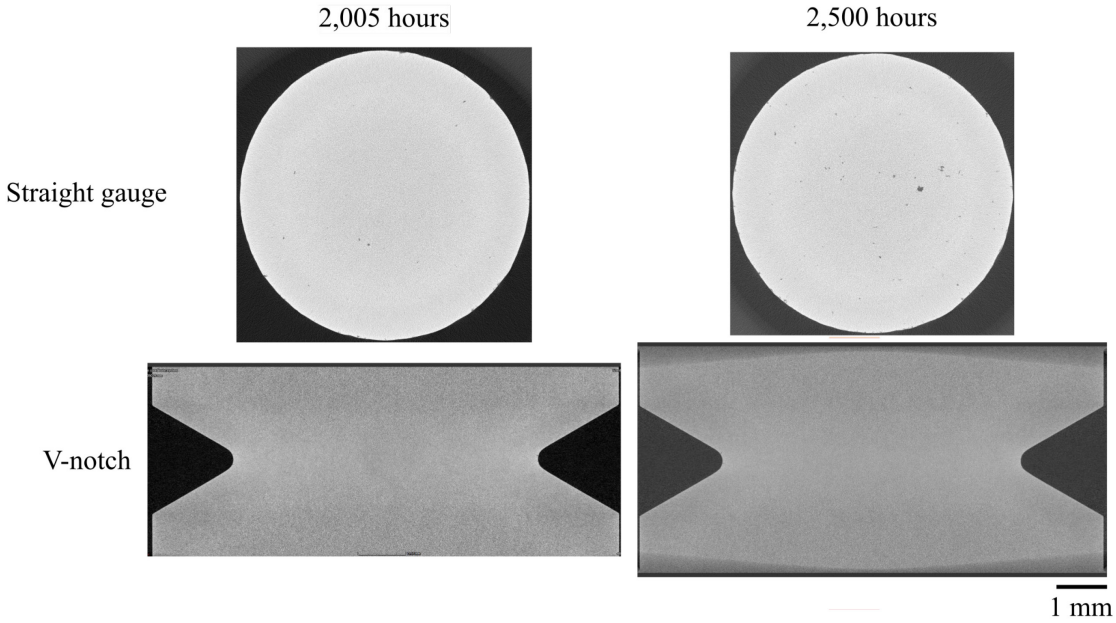

Figure 24: Representative images from X-ray CT scans at 2,005 and 2,500 hours of an ongoing base-metal V-notch creep-rupture test at 800°C and 65.3 MPa. The test has an estimated rupture life of 4,800 hours.

The absence of a validated design methodology for weldments was also flagged by the NRC-sponsored assessment as needing addressed (Huddleston, 1993). Currently, the weldment creep-fatigue procedure in Section III, Division 5 of the ASME BPVC utilizes the base-metal creep-fatigue procedure with additional conservative stipulations. These include reducing the number of fatigue cycles at weldments to a half of the design cycles allowed for base-metal (ASME, 2019, Division 5). The goal of this project is to produce creep-fatigue data of weldments to evaluate the current weldment creep-fatigue procedure. The welded Alloy 617 plates with Alloy 617 filler to be used in this work were inspected with radiography at two different angles. This inspection technique is specified in section b part 3 of HBB-5210 of Section III, Division 5 (ASME, 2019, Division 5). The plates have been confirmed to pass radiographic acceptance standards stated in NB-5320 in Section III, Division 1 (ASME, 2019, Division 1). An iBuy request have been submitted to have cyclic weldment specimens machined from these plates.

The creep-rupture properties of Alloy 800H gas tungsten arc welded (GTAW) with Alloy 617 filler are currently being evaluated. The purpose of this testing is to understand the impact of an overmatched weld. Currently, Section III, Division 5 of the ASME BPVC limits the filler of Alloy 800H welds produced by GTAW to Alloy 82, a matching weld. A service life up to 300,000 hours is permitted. The stress-rupture factors (SRFs) with Alloy 82 filler are small at elevated temperature and long service life (ASME, 2019, Division 5). There is a desire to extend the service life of Alloy 800H to 500,000 hours which will necessitate extending the SRFs. Use of Alloy 800H may be impractical if the stress-rupture factor becomes even smaller with an extension in service life. Alloy 617 filler may offer improved SRFs compared to Alloy 82; this would be beneficial for the extension of Alloy 800H to a 500,000 hour service life. Four creep-rupture tests have been ongoing this quarter. The applied initial stress for three of the tests is estimated to result in a 2,000 hour rupture life for Alloy 800H base-metal. The test temperature is at 700, 750, and 800°C. One test is at 800°C with an applied initial stress estimated to result in a 10,000 hour rupture life for Alloy 800H base-metal. In order to better understand the rupture behavior, the as-

received welded plate is in the process of being characterized. The grain size as a function of distance from the weld was measured using the comparison technique in ASTM E112 (ASTM, 2013). Grain size in the base-metal did not vary with distance from the weld and was an ASTM grain size of 2.

Of the six heat exchanger designs being considered for the intermediate heat exchanger, five require diffusion welding for fabrication (Sabharwall, 2013). Elevated-temperature mechanical-property data are necessary for possible Section III, Division 5 code qualification. Alloy 617 was selected for this investigation as it is the preeminent candidate material for the gas-cooled reactor intermediate heat exchanger.

The creep behavior of the diffusion-welded metal was characterized and compared to creep behavior of fusion-welded and base-metal. The stress exponent, n, from the phenomenological equation was calculated to be in the range of 5.7 to 6.7; see Figure 25. This corresponds to five-power creep, indicating that dislocation climb rate limiting. The base-metal also falls in the five-power creep regime. No conclusions can be drawn regarding the fusion weld since it is metallurgical discontinuity consisting of both base and weld-metal. The activation energy, Qc, was also calculated for the diffusion-welded and base-metal. The diffusion-welded and base-metal were calculated to have similar activation energies of approximately 400 kJ/mol. This is on par with the 410 kJ/mol activation energy reported in the literature for Alloy 617 base-metal (Benz, 2014). The fact that the base and diffusion-welded metal have an equivalent stress exponent and activation energy indicate that they creep in the same manner. This suggests that the interface quality of the diffusion welds are causing the difference in creep-rupture life shown in the Larson-Miller plot in Figure 26. This figure shows the time to rupture Larson-Miller Curve from the Alloy 617 ASME BPVC Section III, Division 5 code case (Wright, 2015). The following data is overlaid: 1) creep-rupture data of base-metal uniaxial data of known chemistry compiled from multiple heats and product forms and 2) diffusion-welded creep-rupture data tested at INL and KAERI.

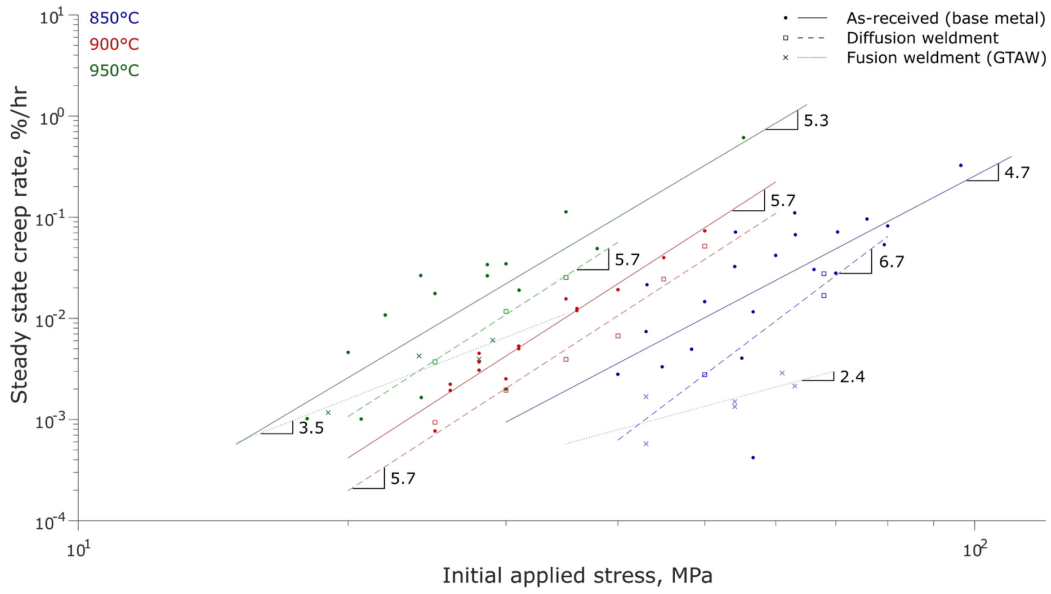

Figure 25: The steady state creep rate versus the initial applied stress for the diffusion-welded, fusion-welded, and base-metal. The slope corresponds to the stress exponent, n.

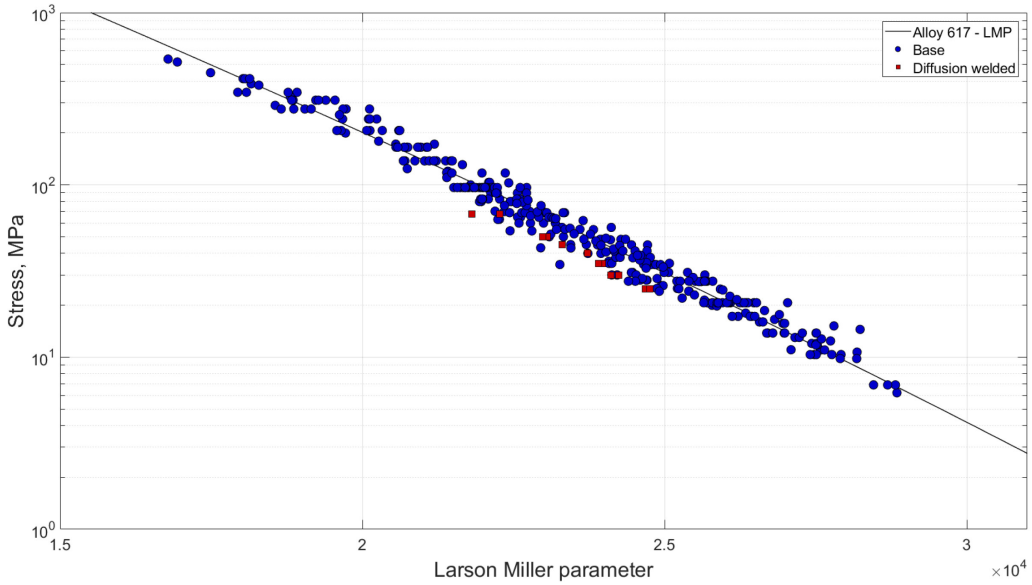

Figure 26: The time to rupture Larson-Miller Curve from the Alloy 617 ASME BPVC Section III, Division 5 code case with the following creep-rupture data overlaid: 1) base-metal uniaxial data of known chemistry compiled from multiple heats and product form, 2) diffusion-welded data.

The creep and cyclic data performed at INL and KAERI were analyzed with respect to Section III, Division 5 of the ASME BPVC. This entailed looking at the SRFs and D-diagram. The following limitations were placed on the SRFs analysis: 1) the temperatures were limited to the diffusion-welded creep test temperatures and 2) the time extrapolation was limited to a factor of five times longer than the longest diffusion-welded creep-rupture test at each temperature. The SRFs were calculated by determining the stress for a given temperature and time to cause rupture in the diffusion-welded and base-metal. These stresses were determined from a regression analysis fit to the diffusion-welded data for the former. The latter was determined using a regression analysis calculated by Wright fit to data from 296 creep specimens of known chemistry used for the Section III, Division 5 code case (Wright, 2015). The resulting SRFs are shown in Figure 27. Wright's report describes a decrease in creep-rupture life for contemporary heats of Alloy 617 which she attributes to a decrease in cobalt concentration. The diffusion-welded Alloy 617 has a cobalt concentration consistent with the contemporary heats. Therefore, the calculated SRFs instead of solely capturing the impact of diffusion welding, as desired, may be additionally picking up on chemistry effects. Consequently, the SRFs were recalculated using a regression analysis for the base-metal from a single contemporary heat with a low cobalt content. This heat had 38 creep-rupture specimens. The recalculated SRFs are also presented in Figure 27. The diffusion-welded data was also calculated and plotted on the Alloy 617 D-diagram; see Figure 28. INL's diffusion-welded contributions were included in a report and presentation for final reporting of I-NERI 2016-002-K, Demonstration of Diffusion Bonding Performance of Alloy 617 for the Application of Compact Heat Exchanger.

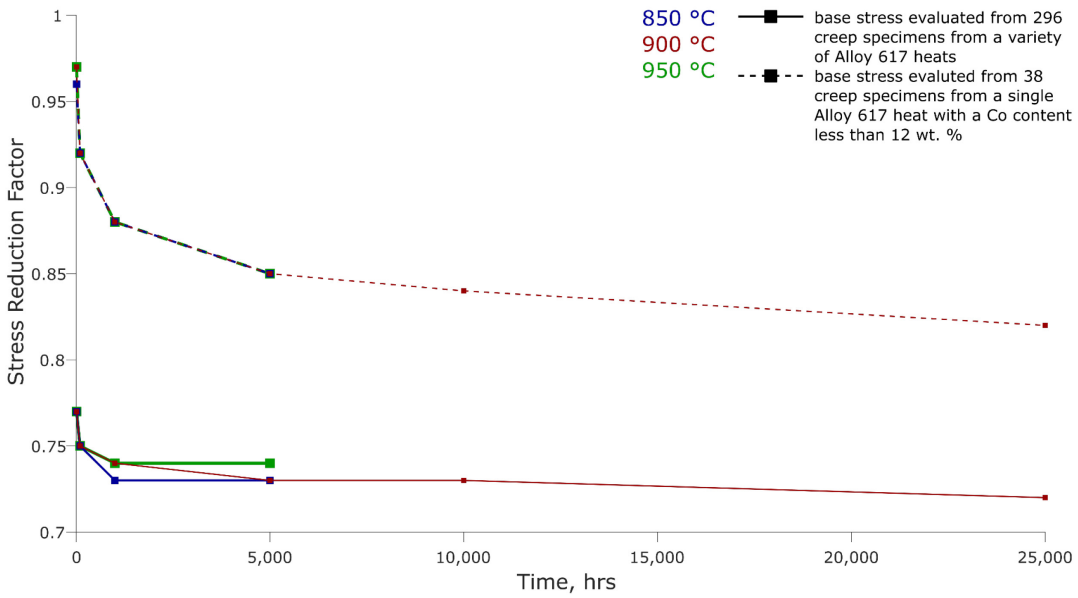

Figure 27: SRFs for the diffusion-welded metal as function of time.

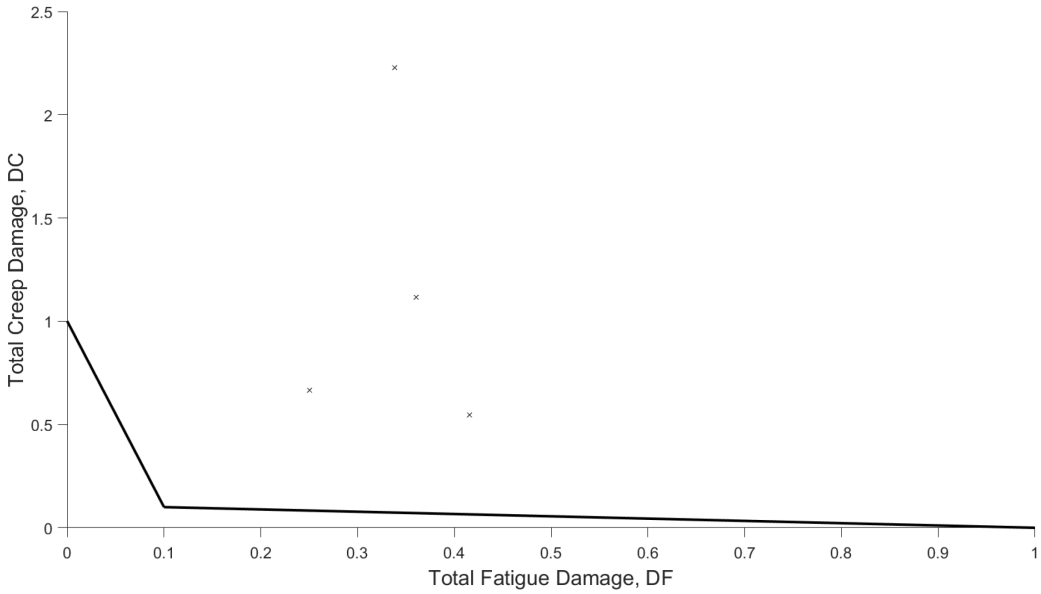

Figure 28: The diffusion-welded data plotted on the D-diagram. The solid lines are the Alloy 617 creep-fatigue envelope from Code Case N-898.

2.2.1 References

ASME. 2019. BPVC- Section III, Division 1. New York, NY.

ASME. 2019. BPVC- Section III, Division 5. New York, NY.

ASTM Standard E112. 2013. *Standard Test Methods for Determining Average Grain Size.* West Conshohocken, PA: ASTM International.

Benz, J. K., Carroll, L. J., Wright, J. K., Wright, R. N. and Lillo, T. M. 2014. "Threshold Stress Creep Behavior of Alloy 617 at Intermediate Temperatures." *Metallurgical and Materials Transactions A* 45: 3010-3022.

Huddleston, R. L. and Swindeman R. W. 1993. *Materials and Design Bases Issues in ASME Code Case N-47*. NUREG/CR-5955; ORNL/TM-12266. Oak Ridge, TN: Oak Ridge National Laboratory.

Natesan, K., Li, M., Soppet, W. K., and Rink D. L. 2012. *Creep Rupture Testing of Alloy 617 and A508/533 Base Metals and Weldments.* ANL/EXT-11/46; TRN: US201202%%897. Argonne, IL: Argonne National Laboratory.

Sabharwall, P., Clark, D. E., Mizia, R. E., Glazoff, M. V., and McKellar, M. G. 2013. "Diffusion-Welded Microchannel Heat Exchanger for Industrial Processes." *Journal of Thermal Science and Engineering Applications* 5: 011009-1 – 011009-11.

Wright, J. K., Carroll, L. J., and Wright, R. N. 2014. *Creep and Creep-Fatigue of Alloy 617 Weldment*. INL/EXT-14-32966. Idaho Falls, ID: Idaho National Laboratory.

Wright, J. K. and Lillo, T. M. 2015. *Progress Report on Alloy 617 Time-Dependent Allowable Stresses.* INL/EXT-15-35640. Idaho Falls, ID: Idaho National Laboratory.

2.3 Graphite Development and Qualification

2.3.1 Materials: Graphite

2.3.1.1 INL Baseline Characterization

Two baseline testing ECAR documents were issued in December 2019, completing two Level 2 Milestones. Baseline Characterization Database Verification Report – IG110 Billet 10X69 and Baseline Characterization Database Verification Report – 2114 Billet A20570 provide control charts for results from a comprehensive array of testing. Fracture categorization plots from each are shown together in Figure 29.

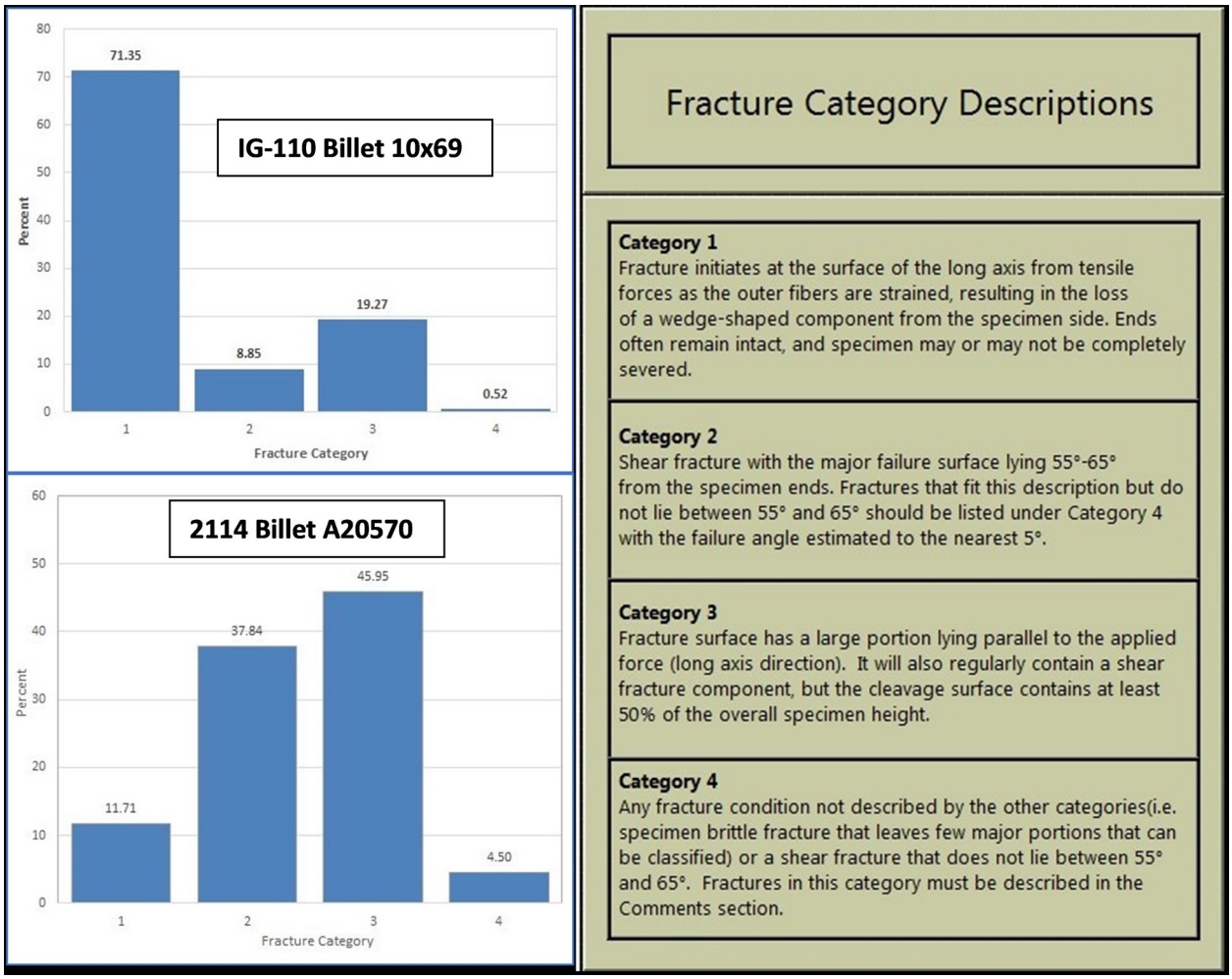

Figure 29. Categorization and distribution of observed fractures from characterization of IG-110 Billet 10x69 and of 2114 Billet A20570.

2.3.1.2 ORNL Baseline Characterization

Two 6-mm-diameter x 3-mm-thickness discs have been machined from the heads of 24 type 109 ASTM C749 (dog-bone) broken tensile specimens, thus yielding a total of 48-disc specimens. The C749 specimens were all from the center slab of Mersen grade 2114 billet (No. 116310). Previous testing established that grade 2114 graphite could be considered isotropic, thus the perpendicular orientation (to the C749 fracture) of the discs expected fracture should not matter. The duplicate specimens will be used for future determinations of the effect of chronic oxidation on tensile strength.

One each of the pair of discs (24-disc specimens) has been examined per ASTM D8289 (Tensile Strength Estimate by Disc Compression) to determine its dimensions. The specimens were additionally weighed, and the density ascertained. The mean density was determined to be 1.81 $g.cm^{-3}$. A value that is identical to the manufactures reported density for grade 2114 graphite.

The 24 Brazilian disc specimens are currently awaiting mechanical testing. The data will allow comparison of the tensile strengths determined from the two-test geometries.

2.3.1.3 Graphite Modeling

The intent of this work is to develop a model capable of predicting the fracture behavior of virgin nuclear graphite from a set of experimentally determined microstructure parameters. A typical graphite microstructure contains pores, filler particles and binder material. Work this quarter can be broken into two main activities: (1) investigation of the effect of variability in pore structure and (2) implementation of circular filler particles.

The pore distribution in multiple graphite grades have been characterized and are available in the literature. The mechanical behavior of graphite, like most ceramics, has significant variability and should be represented by a distribution. To study the effect of a variable pore structure, the distribution employed by Chakraborty[b] is implemented here. More specifically, circular pores with a lognormal size distribution are randomly distributed. Three example pore structures are shown in Figure 30.

Figure 30. Example pore structures approximation for graphite grade H-451.

In these simulations, the filler and binder are not differentiated and are considered to be isotropic. During a simulation, a constant strain rate is applied which causes the evolution of the damage phase (crack growth). An example of the damage phase at the start and end of a simulation as well as the stress versus strain relation are shown in Figure 31. The stress versus strain plot shows the expected quasi-brittle behavior.

Seventy simulations were run with variable pore structures. The ultimate tensile strength was found to have a mean and standard deviation of 16.4 and 1.84 MPa respectively. This matches well with the experimental values of 16 and 1.6 MPa found in Burchell[c]. However, the simple setup of this procedure is not generally applicable because these simulations used microstructurally dependent parameters taken from experiment. As this was only tested for and against H-451, this procedure may not match as well for a different graphite grade. In either case, a model capable of predicting behavior from microstructure alone requires additional inputs.

[b] P. Chakraborty, et al. "A phase-field approach to model multi-axial and microstructure dependent fracture in nuclear grade graphite," Journal of Nuclear Materials, Vol. 475, pp. 200-208, July 2016.

[c] T. Burchell, "A microstructurally based fracture model for polygranular graphites," Carbon, Vol. 34, Issue 3, pp. 297-316, 1997.

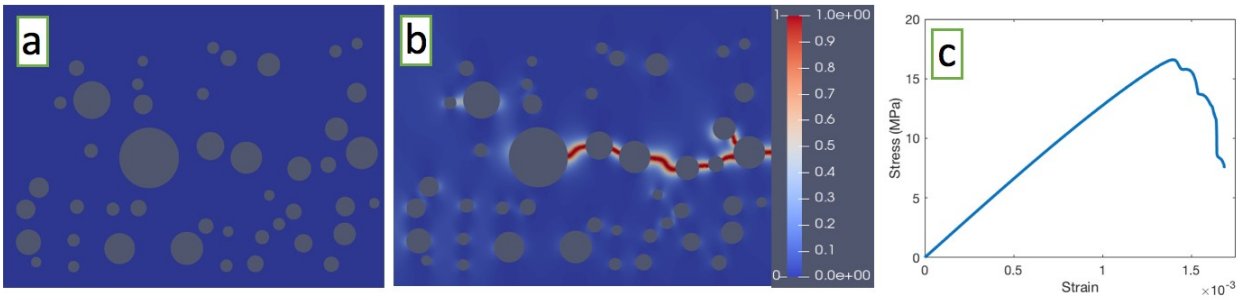

Figure 31. (a) H-451 pore distribution, (b) damage phase at the end of the simulation, and (c) stress versus strain during simulation.

Simulations were run which implement the microstructural features for NBG-18 presented in Kane[d]. Kane's microstructural characterization included distribution parameters for the size and shape of the pores as well as filler particles. A distinction between filler and binder material is important because it will affect the crack behavior due to the difference in the filler's and binder's elasticity tenors. The left image in Figure 32 shows an example of the approximated NBG-18 microstructure where the gray ellipsoids are pores and the colored circles are filler particles. The simulation proceeds by fixing the bottom boundary nodes and applying a positive velocity to the top boundary nodes. The right image in Figure 32 shows the simulated damage phase (crack) and scale bar.

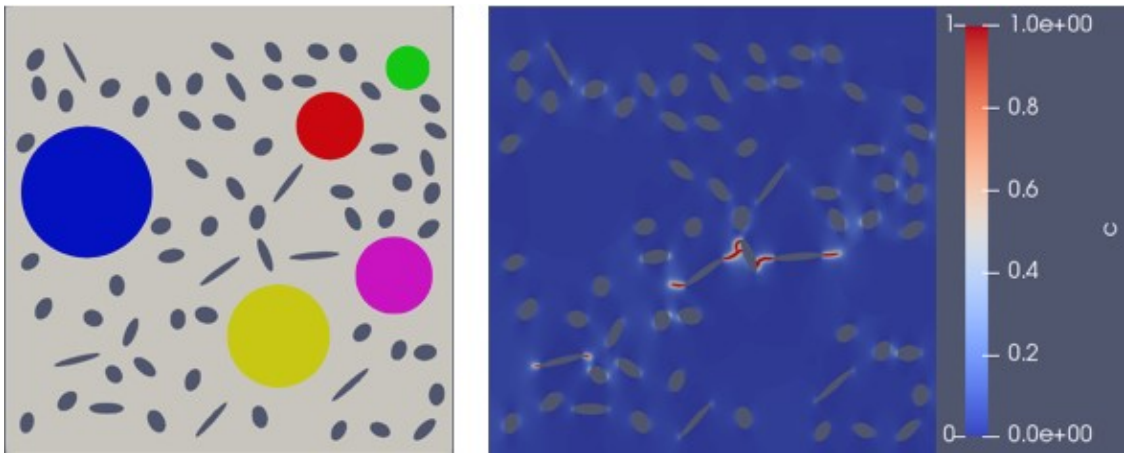

Figure 32. Approximated NBG-18 microstructure (left) and phase field fracture simulation (right).

2.3.2 Collaborations and Licensing: Graphite

2.3.2.1 ASME and licensing

2.3.2.1.1 ASME/NRC Roadmap

The NRC is tasked to review and address code relevant issues to enable industry with technology role out that requires licensing. The ASME-NRC's roadmap efforts will be supported by INL and ORNL. This work relevant to graphite materials is limited to the 2017 Edition of the ASME BPVC Section III Division 5, with reference to the nonmetallic core support structures section, which only include rules for graphite materials.

[d] J. Kane, et al. "Microstructural characterization and pore structure analysis of nuclear graphite," Journal of Nuclear Materials, Vol. 415, pp. 189-197, 2011.

The intention of the roadmap is to enable the NRC with their review by providing a summary whitepaper report on the background information (the basis of the nonmetallic rules) and a summary whitepaper report on the potential gap assessment that will focus on whether the current Division 5 Code rules provide reasonable assurance of adequate protection against identified structural failure modes with respect to argued issues.

The purpose of the whitepaper report titled "ASME Division 5 Nonmetallic Rules Background" is to provide background information on the scope, development, and verification of the elevated temperature design and construction rules in "ASME Section III, Division 5, Subsection HH, Class A Nonmetallic Core Support Structures, Subpart A Graphite Materials, 2017 Edition." The draft discusses the graphite design methodology and how it differs from metallic components. It refers to previous design basis documentation and discuss the underlying methodology for graphite design codes.

The drafted document was internally reviewed. After concerns were addressed to ensure the document is open sourced and within the public domain, the revised draft was distributed for external review. Feedback from external review is pending.

Additionally, a criteria document, drafted by the Graphite and Composite Design Working Group (now called the Nonmetallic Design and Materials), is in the process of being converted to a NTB that will be supplementary to the effort. Similarly, the document is to be revised to contain sources available to the public.

2.3.2.1.2 ASME Code Development

ORNL Staff prepared for and participated in several working and subgroup meetings of the ASME Code Week event during the last week of October held in Atlanta, Georgia. The activities included chairing the Nonmetallic Design and Materials (NDM) working group (WG) where new code additions, revisions and industry interest on topics relevant to the design of High Temperature Reactor Nonmetallic Core Support Structures for Graphite Materials (Section III, Division 5, Subsection HH, Subpart A) and Composite Materials (Section III, Division 5, Subsection HH, Subpart B) were addressed. Other participation included the WG General Requirements for Graphite and Ceramic Composite Core Components and Assemblies (GR GCCCCA), the High Temperature Reactors Stakeholders, and feedback reporting to Subgroup High Temperature Reactors (BPV III).

During the first quarter of FY-20, a requirement was raised to revise the BPVC companion guide that includes description on graphite (section 17.5). Additionally, a few corrections are being introduced to eliminate potential confusion regarding fluence and dose terminology as well as some text to clarify the rules regarding elevated temperature testing. These updates are being reworked and will be discussed at the next meeting in February. Efforts to adopt a code case and code change which replaces grain size with the process zone size in the finite element method (FEM) cell size is ongoing.

2.4 GRC Modeling & Validation

2.4.1 Experimental Validation

Qualified experimental test data from the Oregon State High Temperature Test Facility along with associated documentation was received and stored on the NDMAS system at the INL. Supporting documentation included the Test Analysis Report, Instrumentation locations, and facility description for each test. The INL Property Management Department has initiated contact with Oregon State to transfer the HTTF equipment to the university.

2.4.2 HTGR Methods Core Simulation

The HTGR Methods Core Simulation Work Package did not receive any new funding in FY20, and the activities are limited to the completion of the IAEA CRP on the HTGR Uncertainty Analysis in

Modeling (UAM) and the development of improved simulation methodologies utilizing FY19 carry-over funding.

2.4.2.1 IAEA CRP on HTGR UAM

The IAEA launched the CRP on HTGR UAM in 2013 to study uncertainty propagation in the HTGR analysis chain. Two benchmark problems are defined, with the prismatic design represented by the GA MHTGR 350 (led by INL) and a 250 MW modular pebble bed design similar to the HTR Pebble Bed Module (PM) (led by INET, China). The CRP was formally concluded in 2019, and the drafting of the summary technical document (TECDOC in IAEA terms) will start in February 2020. It is expected that the TECDOC will be completed in 2021.

INL will provide input to the comparisons of the data sets provided by participants for Phase I (lattice simulations) and Phase II (core simulations). The benchmark initially set out to compare uncertainty assessment methodologies and results for neutronics and thermal fluid steady state and transient simulations, but due to limited funding and resource constraints most participants only completed the neutronics assessments defined for Phase I. INL, North Carolina State University (NCSU) and KAERI produced results for Phase II, but only INL completed coupled transient assessment of both the neutronics and thermal fluid domains.

An example of the typical data produced by the INL codes PHISICS/RELAP5-3D as part of this CRP is shown in Figure 33. The figure shows the time-dependent heat-up and cooldown of the MHTGR-350 core during a pressurized loss of cooling (PLOFC) event for two core models containing 0% and 11% bypass flows. Since a statistical uncertainty propagation method has been used, the mean and standard deviation for 1,000 PLOFC transients are presented in Figure 33. Several input parameters were perturbed based on their statistical uncertainty distributions, e.g., uncertainties in thermal conductivity, specific heat capacity, total power, mass flow rates etc. were taken into account. The mean values of the two data sets are obtained from the 1,000 fuel temperature values obtained for each of these perturbed steady state and transient models. The first 200 samples of the 0% bypass flow model perturbations are shown in Figure 34. The main figure of merit is the standard deviation, i.e., the impact of these input uncertainties on the PLOFC maximum fuel temperature. It can be seen than for these two models the maximum fuel temperature standard deviation remains less than 0.15%, which is well within the typical uncertainty margins tolerated by HTGR core designers.

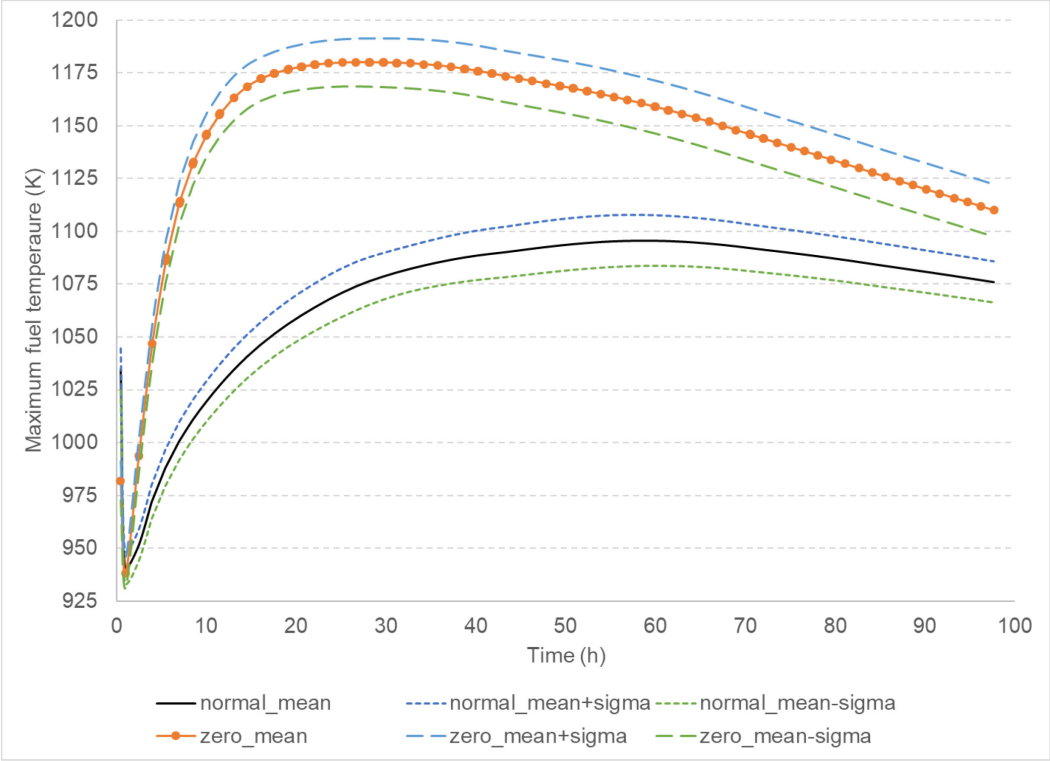

Figure 33. Comparison of core maximum fuel temperature mean and ± one standard deviation values for the 0% and 11% bypass flow scenarios.

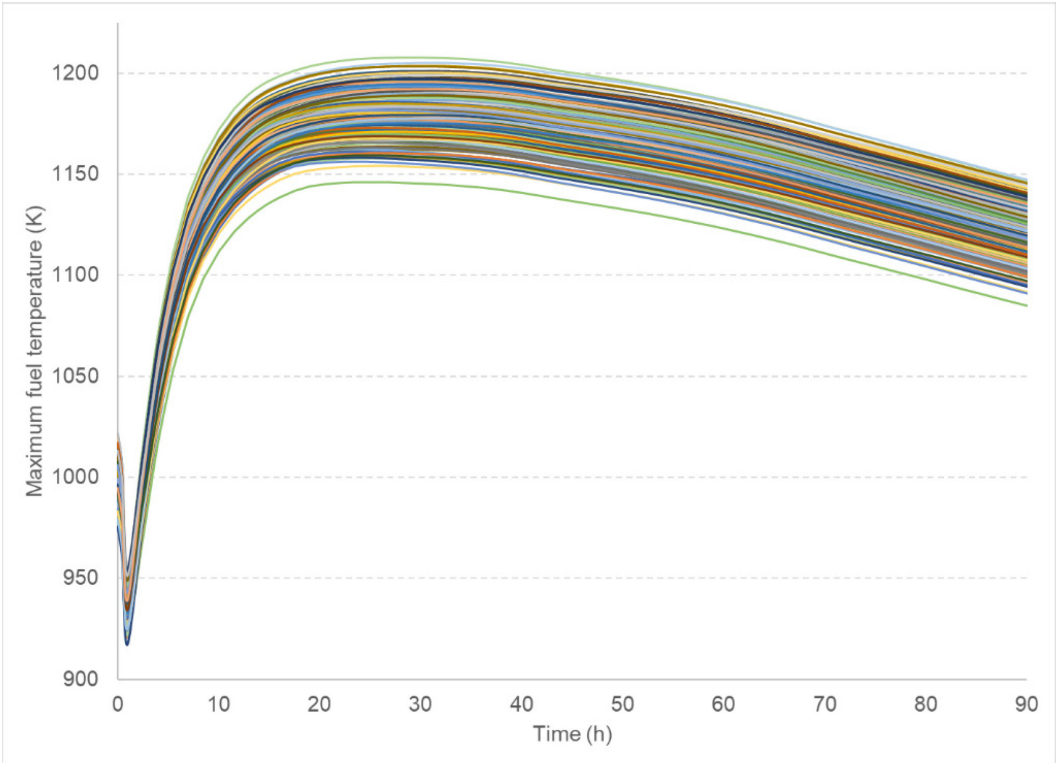

Figure 34. Maximum fuel temperature (K) values for perturbed samples 1-200 of the 0% bypass flow model.

2.4.2.2 HTGR Core Simulation Methodology Development

Pebble bed HTGR cores have moving fuel and in multi-pass loading schemes different pass pebbles at different burnups are mixed inside the core. There are multiple heterogeneities like the double heterogeneity inside the fuel and the control rods being outside the core. The spectral zones if selected properly to account for the temperatures and materials are small enough that the leakage between them needs to be taken into account. The cross sections have strong temperature dependence and the temperature differences are large. On top of these, the isotopic composition within each pass pebble in each zone needs to be predicted in the fuel zones and the challenge for pebble bed HTGR core simulation for equilibrium analysis lies in the coupling of pebble motion and recirculation, nuclide transmutation and neutron energy spectra.

Traditionally, the spectral zones are chosen using engineering judgement, either tabulated cross sections as a function of the parameters given in PBMR400 Benchmark is used or online slowing-down calculations are performed, which requires longer runtimes. The leakage terms are obtained from the few-group bucklings or albedos computed in the core diffusion calculations. These methods and tools have been validated against critical experiments but the uncertainties and required engineering judgement are still significant.

The proposed work consists of using some of the traditional state parameters, such as fuel and graphite temperature and xenon concentrations, however, instead of using bucklings in few-groups we're going to use current dependent leakages. We're also going to include the burnup dependence to the few-group cross sections. It is not straight forward since different minor actinide and fission-product content is possible in separate pebbles at same burnup depending on the trajectory of the pebbles through the core. Therefore, a new state parameter will be introduced using spectrum indices such as U235 fission to U238 capture ratio.

- Attended the Technical WG meeting on HTGRs in IAEA headquarters in Vienna.
- Attended the Technical Meeting on the Competitiveness and Early Deployment of Small Modular Reactors and High Temperature Gas-Cooled Reactors in IAEA Headquarters in Vienna.
- Continued support of the computation methods validation board.

3. 90 DAY LOOK AHEAD

3.1 Important Activities

3.1.1 Fuels Development

- Completed and issued new report "AGR-2 Compact 6-4-1 Post-Irradiation Examination Results" (INL/EXT-18-45418).
- Completed and issued revision to report "Fission-Product Inventory and Burnup Evaluation by Gamma Spectrometry of the AGR-2 Irradiation" (INL/EXT-16-39777, Rev. 1).
- Completed and issued revision to report "AGR-2 Irradiation Experiment Fission-Product Mass Balance" (INL/EXT-19-53559, Rev. 1).
- Packaged and shipped AGR-3/4 Capsule 12 inner and outer rings samples to PNNL.
- Performed re-irradiation and heating testing of cracked particles from AGR-2 Compact 2-2-1.
- Completed TEM data analysis on particle AGR2-222-RS027.
- Planned FIB sample preparation of two new AGR-2 TRISO particles for FY-20 TEM work.
- Presented recent results on TRISO work at TMS 2020 conference (February 23–27) in San Diego.

- Residual AGR-1, AGR-2, and AGR-5/6/7 kernels and TRISO particles at BWXT will be shipped to and archived at INL.
- Some of the unusable uranium-bearing materials at BWXT from the AGR fuel development program will be shipped for disposal.

3.1.2 High Temperature Materials

- Participate in the February 2020 ASME BPVC Week.
- Sustained ongoing creep-rupture tests. These specimens included the Alloy 800H weldments with Alloy 617 filler and the Alloy 617 containing various geometric discontinuities. The data will be analyzed as tests finish. Metallography and optical microscopy will be used to characterize specimens of interest.
- Reloaded and restarted the baseline creep-rupture test (800°C, 65.3 MPa) of a base-metal Alloy 617 V-notch specimen. The test will be interrupted every 500 hours for x-ray CT characterization.
- Started and sustained a baseline creep-rupture test (800°C, 60 MPa) of a base-metal Alloy 617 V-notch specimen. This test will be paused periodically for x-ray CT characterization.
- Started and sustained an 850°C creep-rupture test of a cross-weld specimen with Alloy 800H base-metal and Alloy 617 filler with a targeted rupture life of 2,000 hours.
- Characterized the hardness as a function of distance from the weld for the as-received Alloy 800H welded plate with Alloy 617 filler in order to determine if a heat affected zone is present.
- Started and sustained creep-testing of the diffusion-welded plate for a collaboration with Australia's Nuclear Science and Technology Organization.
- Draft and submit a conference proceeding for the ASME Pressure Vessels and Piping conference.
- Draft and officialize a statement of work for the machining of base-metal double V-notch Alloy 617 specimens.
- Submit an iBuy request to have base-metal double V-notch Alloy 617 specimens machined.

3.1.3 Graphite Development and Qualification

- Issue memorandum, "Status of oxidation studies on irradiated graphite" (Level 3 Milestone) by February 29, 2020.
- Attended ASME BPVC week (Feb. 2–7, 2020) in Las Vegas, Nevada, and reported ASME/NRC Roadmap efforts and modifications to graphite ASME code development. Participated in the working groups for Nonmetallic Design and Materials and for General Requirements for Graphite and Ceramic Composite Core Components and Assemblies (W. Windes and W. Geringer).

3.1.4 GRC Modeling & Validation

- Performed a scoping RELAP5 assessment calculation using existing HTTF model developed and compare results to selected HTTF Matrix Test data.
- Continued discussions with INL property Management organization and OSU about transferring the process to transfer the HTTF equipment to OSU.
- Completed the INL contributions to the IAEA TECDOC on the IAEA CRP on HTGR Uncertainties in Modeling (UAM) and the OECD/NEA MHTGR-350 benchmark comparison report.
- Continued support of participants' results submitted for the IAEA CRP on HTGR UAM, and provide input to the draft summary IAEA TECDOC. the computation methods validation board.